POLITECNICO DI TORINO

Department of Mechanical and Aerospace Engineering

Class LM-21 Degree: BIOMEDICAL ENGINEERING

Master thesis in Biomedical Engineering

Numerical study of displacement forces and energy dissipation in patient-specific post-EVAR hemodynamics models

Supervisor: *Prof. Umberto Morbiducci*
Co-Supervisors: *Dr. Diego Gallo*
Dr. Paola Tasso

Master Student:
Valentina Verteramo

Academic Year 2017-18

Index

Abstract

Abdominal Aortic Aneurysm (AAA) is a localized dilatation of the abdominal aortic lumen due to the degradation of its mechanical properties.

During the last twenty years the endovascular surgery took place as standard practise instead of the traditional open repair surgery that presents an higher morbidity rate and invasiveness. The endovascular devices are used to exclude bloodstream from the dilated vessel portion and compared to the open surgery it has the advantage to does not require open-chest or open-abdominal surgery. Endograft migration and thrombization are the main cause of failure of these devices.

Nowadays, Computational Fluid Dynamics (CFD) became a customary tool to characterize the hemodynamic inside cardiovascular devices.

This master thesis work is focused on the use of CFD, here exploited to evaluate the flow efficiency losses in ten image-based models as reconstructed from subjects treated with EVAR. Technically, the amount of mechanical energy irreversibly converted into internal energy, expressed in terms of Viscous Dissipation Rate (VDR), was calculated from CFD simulations. Displacement Forces (DFs) acting on the vessel wall of the endografts were also evaluated, they are responsible for device migration from implantation site, due to pressure forces, wall shear stress and weight forces acting throughout the cardiac cycle.

VDR, recognised as hemodynamic metric, can be derived from differential energy conservation analysis, following the first thermodynamic law, under which time rate of internal energy variation of a system is equal to the sum of the time rate of transfer heat and the time rate of work done. In this study, power losses and energy losses were investigated and analysed in detail in the specific segments of one commercial endograft model, and its hemodynamic performances were evaluated.

Possible significative associations of the VDR and DFs with other hemodynamic and geometric descriptors that could influence the correct functionality of the device and its stability, were explored. In detail, here the following quantities were considered: (1) geometric features, that a large body of literature suggest to be a promising tool for a

better understanding of the outcome of EVAR procedures; (2) intravascular flow descriptors based on helicity, an indicator of the amount of pitch and torsion in blood flow patterns.

This research provides mean value of energy loss, calculated considering all the entire models, equal to 0.558±0.249 J on all cardiac cycle, whereas considering separately systole and diastole mean values of 0.504±0.222 J and 0.054±0.030 J are obtained respectively, proving that dissipation rate significantly prevails during the initial phase. Similar considerations are made for particular parts of the device, and, in the same way, mean values of energy loss of 0.522±0.231 J, 0.476+0.213 J and 0.046±0.02 J are obtained in the branches, highlighting that the most significant contribution of energy loss always derives from branches.

Analysis of the Displacement Forces generated mean values of 1.580±0.647 N, 1.527±0.622 N and 1.623±0.668 N on all the whole models, producing comparable measures on all the examined periods; equivalent comments can be done for the parts of the devices.

Statistical analysis reveals that any significant relation exists between VDR and DFs. VDR in the total model is related to the variation rate of the area, whereas, regarding the region of the branches, it results associated with the cross-sectional area. Most statistically significant correlation is found between the VDR and the helicity intensity in all the investigations. Displacement Forces appear to be related with geometric descriptors as torsion, curvature and cross-section area, and with hemodynamics descriptors in the branches on systole and diastole.

These study outcomes underline the necessity to analyse, at the design stage, hemodynamics efficiency and geometry features of stent-grafts to optimize them and to predict their long-term stability.

Chapter 1

Introduction to the Cardiovascular System and its main Pathologies

The aim of this chapter is to detect and to describe the principal component of the Cardiovascular System and the Abdominal Aortic Aneurism (AAA) that is one of major cause of death in the modern society.

In the first part, the Heart, the Blood Vessels and the Blood are analysed from a biomechanical point of view, defining their composition and function, in order to find out how they impact the hemodynamic.

In the second section the main pathologies of the arteries are introduced, focusing on the abdominal aortic aneurysm. The risk factors and the expected leading causes are examined to understand how the pathology develops and, consequently, which guidelines has to be adopted to treat it.

Open aneurysm repair (OAR) and endovascular aneurysm repair (EVAR) are considered the most important surgery procedures to intervene on the AAA, so a large part of this chapter is dedicated to describe and compared them.

In Biomechanics, the stent-grafts, employed in EVAR, are of great interest, because of it, they are examined from several point of view. For what concerns this work, the displacement forces, acting on the devices, are investigated in order to determine how they can lead to failure and so to prevent it. The viscous dissipation rate, a measure of mechanical energy loss, is also introduced.

1.1 The cardiovascular System

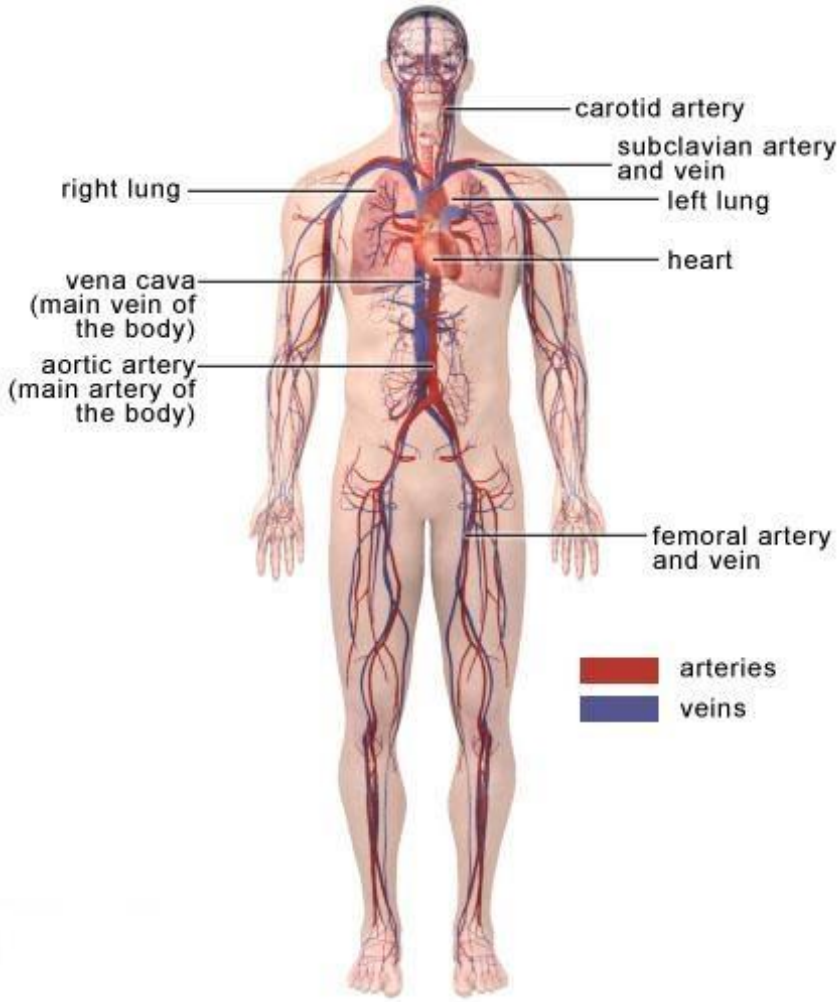

Figure 1.1: cardiovascular system

The cardiovascular system has three major functions: transportation of materials, protection from pathogens, and regulation of body's homeostasis. The cardiovascular system is composed of three principal components, the heart, the blood vessels and the blood. The aim of the cardiovascular system is to transport the blood towards the organs, in order to release oxygen and nourishment substances, and from the organs, taking away the wastes which need to be removed. There are two circulatory loops, the systemic circulation that starts from the left ventricle of the heart, that carry on the oxygenated blood, and the pulmonary circulation from the right ventricle, where the deoxygenated blood reaches the capillaries in the lungs to absorb fresh oxygen and release carbon dioxide.

1.1.1 The Heart

The Heart is a muscular pumping organ about the size of a fist, located medial to the lungs along the body's midline in the thoracic region; its bottom tip is turned to the left. The Heart wall is made of 3 layers: epicardium, myocardium and endocardium[1].

- Epicardium, that is the outermost layer, is a thin serous membrane able to lubricate and protect the outside of the heart.
- Myocardium is the cardiac muscle tissue of the Heart, striated and involuntary, responsible for the pumping blood; it is the thicker layer.
- Endocardium is a squamous endothelium layer that cover the inner cavity of the Heart; it is very smooth to prevent blood sticking to the inside wall and forming potentially deadly blood clots.

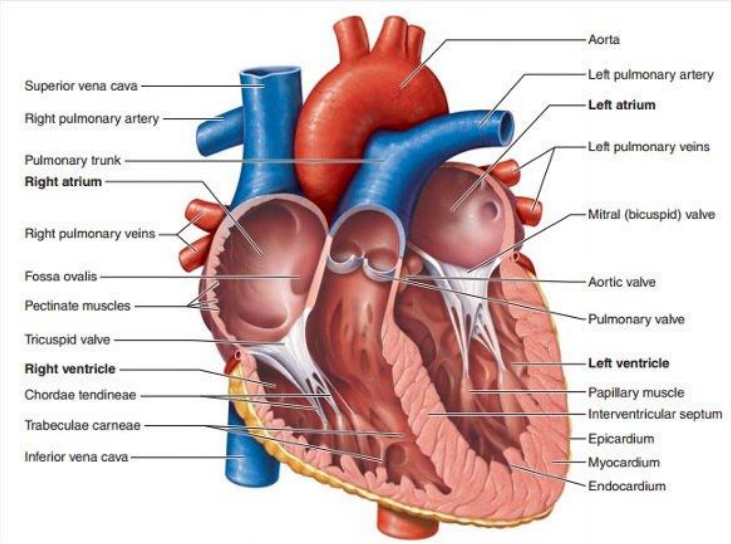

Figure 1.2: heart section

The inner part of the Heart is divided into two closed-off sections, the right section, where deoxygenated blood come in, and the left section, from which oxygenated blood is then pumped through the organs. Each of these sections is split into two chambers, the atrium and the ventricle, through the atrioventricular (AV) valves that allow blood to flow in only one direction, from atrium to ventricle, to avoid regurgitation. The AV valve on the right side of the Heart is called tricuspid valve because of it is constituted of three laps, whereas on the left side is called mitral

valve, or bicuspid valve, because of it has two flaps. Other valves, semilunar valves, so called for the shape of their cusps, can be found between the ventricles and the arteries that carry blood away from the Heart. The semilunar valve on the right side of the Heart is the pulmonary valve, that prevent the backflow of the blood from the pulmonary trunk into the right ventricle, whereas the semilunar valve on the left side of the Heart is the aortic valve, that prevent the backflow of the blood from the aorta into the left ventricle.

1.1.2 The Blood Vessels

The blood vessels are the responsible for the blood transporting toward the tissues and the organs. They can be distinguished into two major categories, the arteries and the veins, the first carry oxygenated blood, the second deoxygenated blood. Arteries have thicker walls and smaller lumen than veins, arterial lumen appears more rounded in cross section than the lumen of veins[2]. In the wall of the veins there is a middle layer of smooth muscle, called tunica media, that is, in general, thinner than those of arteries, because they don't need to contract and to handle high pressures. Most veins are equipped whit valves to prevent reflux.

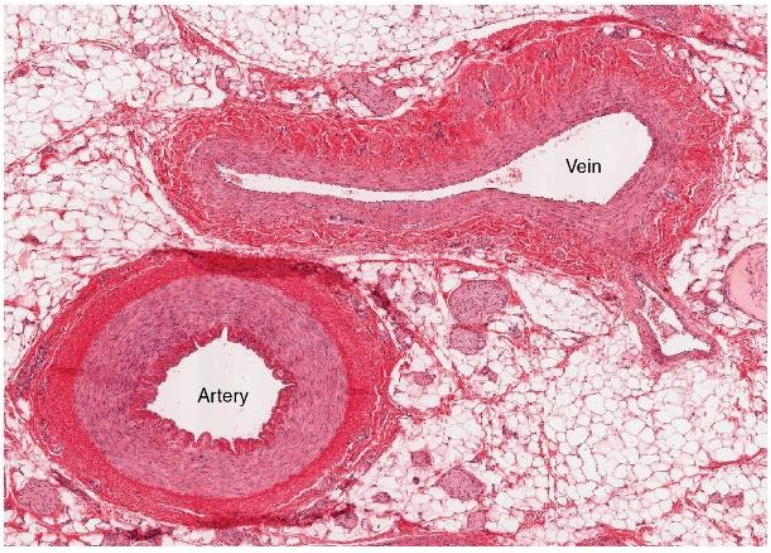

Figure 1.3: artery and vein slices[2]

The arteries are the most relevant and interesting vessels from the biomechanical point of view.

The arteries on the base of their diameter can be differentiated in[3]:

- major arteries, or elastics (i.e. aorta)
- medium caliber arteries, or muscle
- small arteries, with caliber less than 2 mm
- capillaries

The wall of the arteries is composed of distinct tissue layers.

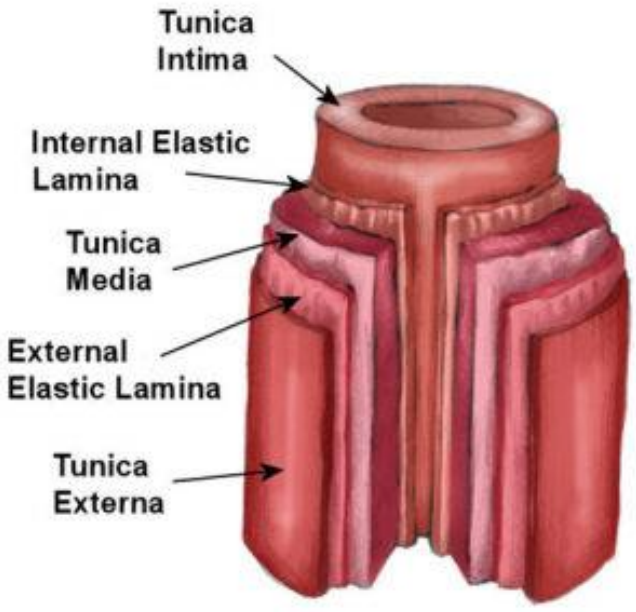

Figure 1.4: anatomy of the arteries

THE TUNICA INTIMA

The tunica intima, the inner layer of the blood vessel, has a single endothelial cells layer, the only non-thrombogenic one, that covers the entire lumen and it is in direct contact with the blood. Damages of the endothelial lining cause clot formation, so laceration can trigger the occurrence of atherogenesis, that leads to atherosclerosis, so the development of atheromatous plaques as a result. The integrity of endothelium is fundamental to maintain the normal structure of the all vessel.

The basal lamina, just below the endothelial lining, is composed of connective tissue, in particular of collagen, elastin and proteoglycans, with thrombogenic effect. It has a structural function, moreover it plays a role of filter, for the exchange between the blood vessel and interstice, this can guarantee nutrient supply for the cells of the vessel and the homeostasis.

THE INTERNAL ELASTIC LAMINA

The internal elastic lamina is composed of elastic fibers placed in longitudinal direction; being fenestrated, in the muscle arteries principally, it permits at the smooth muscle cells to penetrate inside the tunica intima. This structure type allows a kind of migration, that is essential to maintain the homoeostasis, but it is a problem in presence of events out of the physiological condition.

THE TUNICA MEDIA

The tunica media, an alternation of smooth muscle cells and elastic fibers, is poorly vascularized, so the oxygen and other nourishment, needed to carry out the work, came for diffusion from the tunica adventitia, this last one is well vascularized.
There is, in fact, for the major and medium arteries principally, a vascular network, named *vasa vasorum*, wherein the blood flows to perfuse the vessel.
The tunica media is the layer of the vessel responsible for the systolic pulse propagation.
As time goes by, the muscle fibers convert to fibrotic ones, that leads to a change in mechanical properties of the wall, this last one became stiffer, cause high blood pressure and increases the workload of the heart. In physiological condition, the smooth muscle cells govern the vasoconstriction and the vasodilation.

THE TUNICA ADVENTITIA

The tunica adventitia is made of connective tissue, that includes fibroblast, elastic fiber, nerve and vasa vasorum that penetrate no more of one-third the adventitia. Mostly in the medium and small calibre arteries, nervous connections help for vasoconstriction and vasodilation.

THE EXTERNAL ELASTIC LAMINA

The external elastic lamina is similar to the internal one. In percentage, the amount of endothelial cells, elastin, collagen and smooth muscle cells changes from major arteries to capillaries, due to the different role that they play. In the major arteries there is a high presence of elastin, smooth muscle cells and collagen; in the medium calibre arteries increase the quantity of smooth muscle cells, whereas decrease the quantity of elastin and collagen; small arteries and capillaries are predominantly constituted of smooth muscle cells.

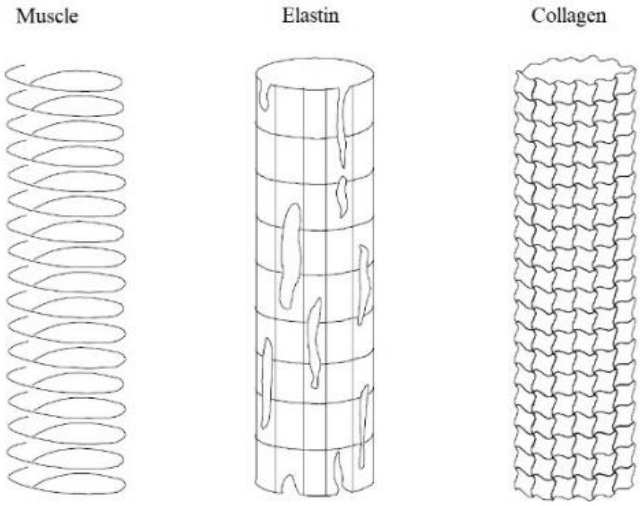

Figure 1.5:structure of the wall components[3]

The most important artery of the circulation system is the aorta, this last one provides oxygenated blood to the whole body in the systematic circulation. It is capable to store mechanical energy in the fist part of the cardiac cycle, whereas in the second part it uses all of that energy to improve diastolic perfusion.
The aorta, directly linked to the left ventricle, extends down to the abdominal region where it splits in two small arteries, the iliac arteries. It is usually divided in different branches:

- *ascending aorta*, located between the left ventricle and the aortic arch, branches into the coronary arteries, responsible for the supply of oxygenated blood to the heart;

- *aortic arch*, the curved portion of the aorta, links the ascending and the descending portions of the aorta, and from which branch off several arteries, like the carotid artery, that supply oxygenated blood to the head, neck region and arms;

- *descending aorta* extends from the aortic arch down to the abdomen, it is composed of the thoracic aorta, that provides oxygenated blood to the chest, oesophagus, bronchi and pericardium, and the abdominal aorta, that provides oxygenated blood to the organs of the abdomen.

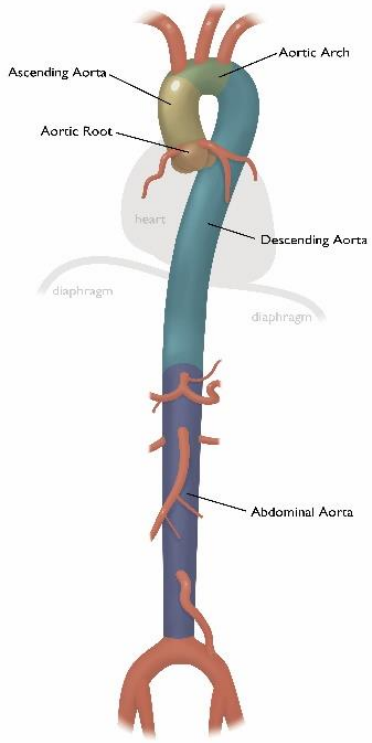

Figure 1.6: aortic branches

Blood Vessel Diseases

The main pathologies that concern the blood vessels walls are the atherosclerosis and the aneurysm, they affect the major and medium arteries primary. In presence of atherosclerosis, the smooth muscle cells, because of non-physiological biochemical pathways, can differentiate in an indiscriminate way, migrating through the tunica intima, invading the lumen of the vessel, so causing the reduction of its section and increasing the resistance to flow. These cells have receptors of the low-density lipoprotein (LDLP), but high molecular weight; the latter insert and store themselves in the filtrating system of the vessel wall, contributing to atheroma formation[3], it has a lipidic core and an external fibrotic capsule.

1.1.2 The Blood

The blood is a connective tissue, flowing through blood vessels, able to perform several functions[3]:

- It carries the oxygen to the tissues, by means of haemoglobin contained in erythrocytes;
- It picks up waste of metabolism, principally carbon dioxide, to ejected them;
- It carries nutrients (i.e. sugar, mineral salts, amino acid);
- It helps to control body temperature;
- It carries hormone, enzymes, vitamins;
- It contributes to organism defence through the white cells;
- It acts in the first phase of the injuries repair through the clotting.

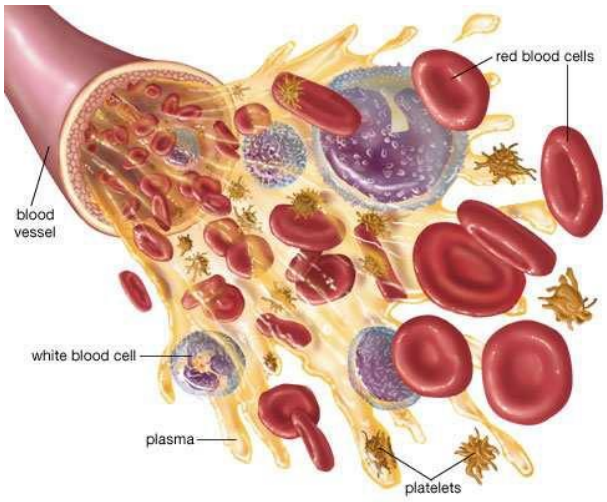

Figure 1.7: blood components [3]

The blood is composed of a fluid part, represented by the plasma, and a corpuscular part, consist of several kind of cells, like erythrocytes, leukocytes and platelets; the percentage in volume of the corpuscular part is called haematocrit (Ht), and its referment value is 0.45.

The plasma is a slightly alkaline fluid, composed of water in which some substances are dissolved, mostly organic substance and some minerals.

The erythrocytes, also called red blood cells, with a diameter of about eight µm are without a core, to be more flexible, having to reach the smallest arteries; they

have biconcave shape and are limited by a membrane called stroma. The red cells contain a considerable amount of haemoglobin, a protein capable of bind oxygen, forming oxyhaemoglobin, fundamental to transport this last one in the blood; the oxygen dissolved in plasma is not enough to fulfil the tissues need. The erythrocytes live between ninety and one-hundred-twenty days, they have to be eliminated before their membrane rupture, in order to be more easily to dispose of by the liver and the spleen.

The leukocytes, the white blood cells, are an aggregation of several elements with spheroidal shape; they are nucleated, so are less deformable of the erythrocytes. They are involved in the organism defence, but in case of pathology, they can change in tumoral blood cells (leukaemia). The leukocytes can be divided in three categories: granulocytes, of granular type, that phagocytise complex antigen-antibody, so they contrast allergens and parasites; lymphocytes, non-granular ones, can be T or B type, they defend the organism from all is felt heterologous; monocytes, precursors of macrophages, are very interesting from biomechanical point of view, because they may interact with the endothelial cells, by contributing to the development of blood vessel pathology.

The platelets, or thrombocytes, have spherical or oval shape, with a diameter of about three μm; they have a short life, of about fifteen days. Platelets take part in two fundamental process: haemostasis, blood clotting and organism defence. In the haemostasis process, the platelets adhere on the lesion site aggregating themselves, and through the secretion of substances call other platelets on the site; the secretion of the serotonin cause the reduction of the calibre of the injured vessels, so the reduction of the flux. The polymerization of the fibrinogen, a protein contained in the plasma, in fibrin produces a kind of network that incorporates the adhere platelets, forming a clot. In pathological conditions, platelets can lead to clots formation, in uncontrollable manner, with a creation of thrombus and cerebral stroke risk as consequence.

Blood Rheology

The rheology studies the flow properties of materials; with regards to blood, it is considered as a homogenous fluid, characterized by two quantities[3]: the density and the viscosity, both dependent on temperature, whereas the viscosity can be also dependent on the state of motion. The state of motion is given by the set of velocity vectors of individual fluid elements.

Blood Density

The whole blood density is strongly dependent of the haematocrit; it is made a primary approximation whereby the blood density is independent of temperature and fluid pressure. It can be computed as:

$$\rho_S = (1 - Ht)\,\rho_P + Ht\rho_{GR}$$

Where ρ_S is the blood density, ρ_P is the plasma density, ρ_{GR} is the red cells density and Ht is the haematocrit, the fraction in volume occupied by red cells, neglecting the other corpuscular part that does not contribute to density definition.

In normal condition:

$$\begin{cases} \rho_P = 1035 \quad kg/mm^3 \\ \rho_{GR} = 1090 \ kg/mm^3 \\ \mathrm{Ht} = 0.45 \end{cases} \quad \rightarrow \rho_S = 1060 \ kg/mm^3$$

Blood Viscosity

The dynamic viscosity represents the internal friction of a liquid, it estimates the sliding resistance and is measured in the I. S. in $N.s/m^2$, so in $Pa.s$; more often it is measured in cP, centipoise, a submultiple of the unit of measurement of the viscosity in the c.g.s. system. [1 cP=$10^{-3}\ Pa.s$]

The viscosity of the whole blood can vary between 3 and 4 cP.

In a Newtonian fluid, the viscosity is independent of the shear rate, it is a physical fluid property and it connects in a linear relation the shear stress and the shear rate:

$$\tau = \mu\dot{\gamma}$$

In a (τ,$\dot{\gamma}$) plot, the dynamic viscosity represents the angular coefficient of the line. In laminar flow condition, in cylindrical straight pipes, the shear rate is only on radial direction, if the fluid flow through x direction the shear stress $\tau = \tau_{xy}$ and the shear rate $\dot{\gamma} = \frac{dv_x}{dy}$.

The blood is a suspension of several parts, it can be considered homogenous only in the major arteries, where the vessel diameter is about 27 mm, whereas the red cell diameter is about 7 µm, bigger four order of magnitude; therefore, inside capillaries, blood cannot be considered homogenous. Moreover, in the major arteries, the blood cannot be considered homogenous for shear rate $\dot{\gamma} < 100\ s^{-1}$, it has not a Newtonian behaviour. For high shear rates, the viscosity is estimated constant, the mechanical forces are such that the red cells cannot aggregate due to the fibrinogen; for low shear rates, the aggregation forces are greater than mechanical forces, so the viscosity is shear rate dependent. During a cardiac cycle, the shear rates can change widely, at the systolic peak, $\dot{\gamma}$ can be five times its mean value in aorta and two times its mean value in smaller blood vessels, whereas during the diastole there are low values of shear rate. Because of the pulsatile flow decreases from the arteries near the heart to the peripheral ones, the shear rate decreases consequently. The blood cannot be considered as a Newtonian fluid, strictly speaking.

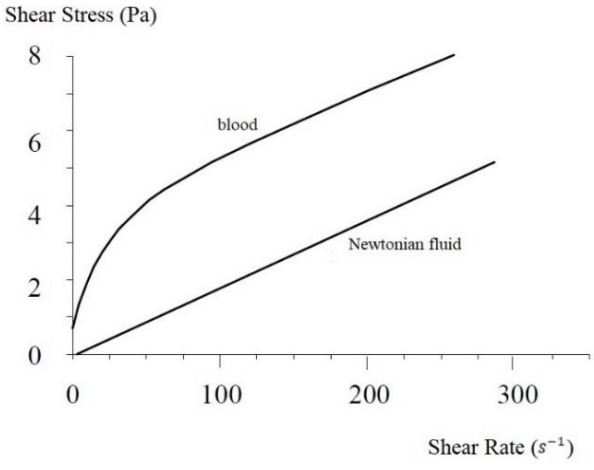

Figure 1.8: Blood and Newtonian fluid viscosity [3]

For a non-Newtonian fluid, the relation between the shear stress and the shear rate is given by:

$$\tau = \mu_{APP}\dot{\gamma}$$

Where μ_{APP} is the apparent viscosity, that is not a physical fluid property because it depends on the state of motion.

Non-Newtonian Rheological Models are explained below:

1. BINGHAM MODEL

The rheological behaviour of the Bingham fluid reflects the rheological behaviour of the blood only for high shear rates. It is given by the equation:

$$\tau = \tau_0 + \mu_B\dot{\gamma}$$

Where μ_B is the viscosity of a Bingham fluid and τ_0 is the yield stress, the minimum shear stress to apply to let the fluid flow.

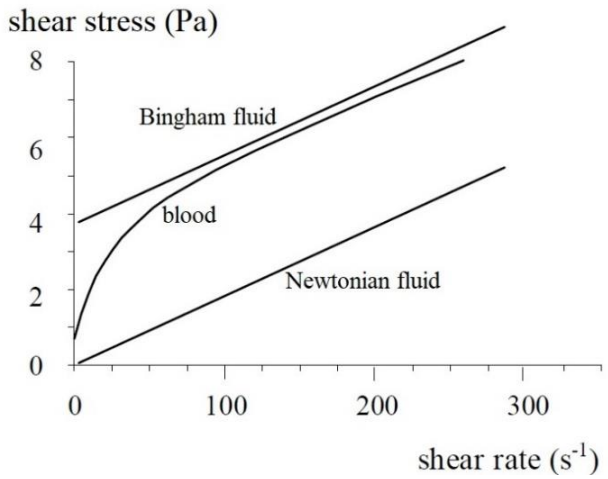

Figure 1.9: behaviour of a Bingham fluid[3]

2. CASSON MODEL

The Casson model is explained by the equation:

$$\sqrt{\tau} = \sqrt{\tau_0} + s.\sqrt{\dot{\gamma}}$$

with s=$\sqrt{\mu_c}$, where τ_0 is the minimum shear stress to apply to let the fluid flow and μ_c is the viscosity of Casson.

3. POWER-LAW MODEL

The Power-Law model links the viscosity, that is dependent of the state of motion, to the state of motion itself.

$$\mu(\dot{\gamma}) = k.(\dot{\gamma})^{n-1}$$

where k is the flow consistency factor and n is the power-law index, that are obtained experimentally.

4. CARREAU MODEL

The Carreau model identifies the shear-thinning property of blood viscosity, it is explained by the equation below:

$$\mu(\dot{\gamma}) = \mu_\infty + (\mu_0 - \mu_\infty)[1 + (\lambda\dot{\gamma})^2]^{n-1}$$

where μ_∞ is the viscosity for $\dot{\gamma}$ tendent to infinity, so when the fluid has a Newtonian behaviour, μ_0 is the viscosity for $\dot{\gamma}$ tendent to zero, λ is the relaxation time constant, it depends on haematocrit, and n is the power-law index.

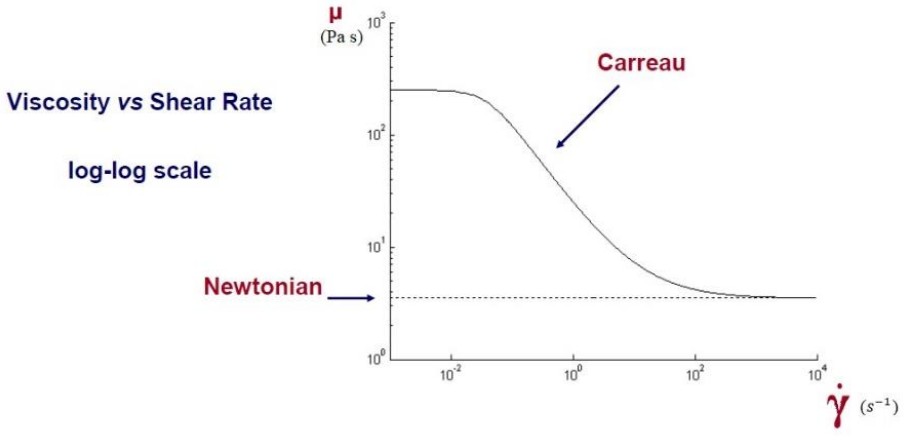

Figure 1.10: viscosity of Carreau[3]

The decay rate of the curve depends on the power-law index and the relaxation time constant.

5. GENERALIZED POWER-LAW MODEL

(Ballyk et al., 1994)

The generalized power-law model is described by the relation below:

$$\mu(\dot{\gamma}) = \lambda(\dot{\gamma}).\dot{\gamma}^{(n(\dot{\gamma})-1)}$$

where $\lambda(\dot{\gamma}) = \mu_\infty + \Delta\mu.\,exp\left[-\left(1+\frac{\dot{\gamma}}{a}\right).exp\left(-\frac{b}{\dot{\gamma}}\right)\right]$

and $n(\dot{\gamma}) = n_\infty + \Delta n.\,exp\left[-\left(1+\frac{\dot{\gamma}}{c}\right).exp\left(-\frac{d}{\dot{\gamma}}\right)\right]$

In this case, the power-law index and the relaxation time constant are both dependent on shear rate. Ballyk et al. have complicated the model to better approximate experimental data.

1.2 Abdominal Aortic Aneurysm (AAA)

The aneurysm is a balloon-like dilatation of the abdominal aorta exceeding 1.5 times its normal diameter[4]; it is considered pathological for infrarenal diameters equal or greater of 3.0 cm.

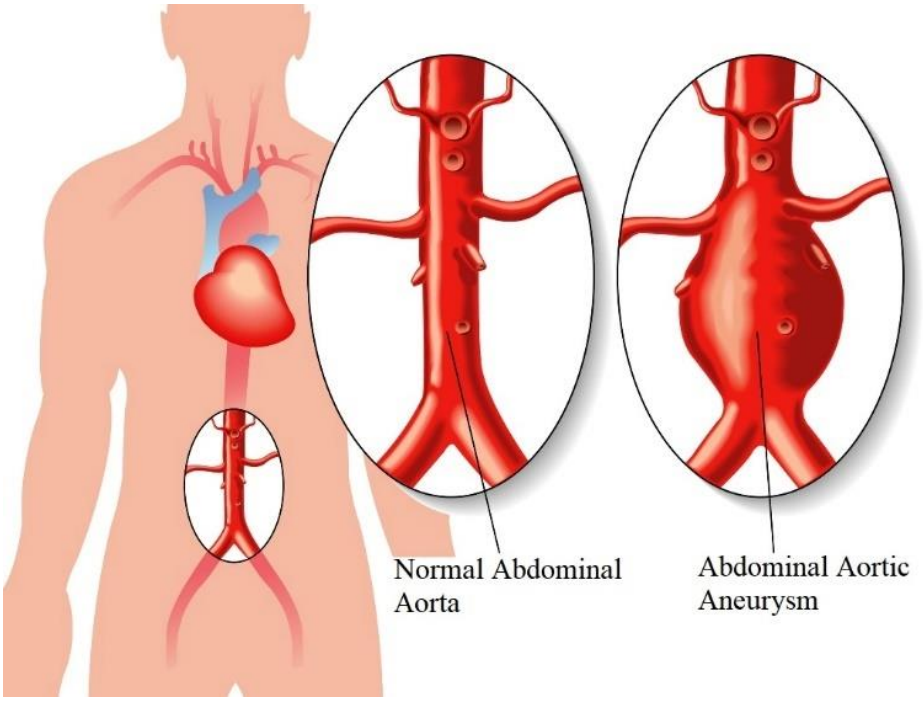

Figure 1.6: Abdominal Aortic Aneurysm

There are two types of aortic aneurysm distinguished by the shape: the fusiform aneurysm, that appears as symmetrical dilatation of the blood vessel, it is more common shape, and the saccular aneurysm that appears as a lateral growth, less common, caused by trauma or aortic ulcers. AAA is evaluated to be the tenth commonest cause of mortality and is responsible for about 2% of all deaths.

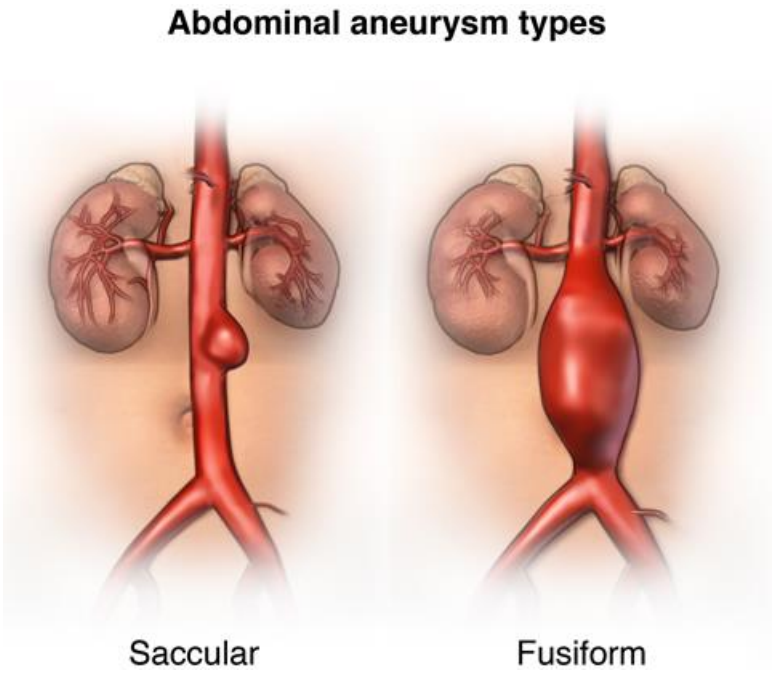

Figure 1.7: Saccular and Fusiform Aneurysm

Prevalence and Risk Factors

Even now, it is not well-understood the events that trigger the initialization and the developing of the disease. Main risk factors may be individuated in age older than 65 years, male sex, smoke, hypertension, previous myocardial infarction, peripheral arteries disease, coronary artery disease and a family history of abdominal aortic aneurysm[5]. Moreover, AAA seem to be more common among Northern European ethnicity than African or Asian. The aneurysm is thought to be a consequence of atherosclerosis, even if this disorder emerges through pathogenic mechanisms that vary, at least in part, from mechanisms responsible for athero-occlusive disease. Moreover, not all patients affect by atherosclerosis develop the aneurysm subsequently, so other factors have to be involved onto aneurysm formation and growth.

Aortic Wall Composition

The aortic wall is composed of elastin, collagen, smooth muscle cells and ground substance, which are responsible for the structural integrity, metabolism and mechanical properties of the aortic wall[6]. Elastin and collagen regulate the passive mechanical properties, whereas smooth muscle cells govern the active mechanical properties. The non-aneurysmal abdominal aortic wall is characterized by distinct lamellar units composed of elastin layers divided by smooth muscle, collagen, and ground substance, whereas in the aneurysmal aortic wall, the medial lamellar units appear to be destroyed, elastin fragmented and most of the muscle disappeared. In most aneurysmal aortic walls, the internal elastin layer was destroyed, it was difficult to distinguish the intima from the rest of the wall. By comparing the wall composition for an aneurysmal abdominal aorta with a non-aneurysmal abdominal aorta, the volume factions of both elastin and muscle cells decrease evidently, whereas the volume fractions of both collagen and ground substance increase, although the ratio of collagen to ground substance remains unchanged[6]. Investigating the mechanical properties of arterial wall through tensile testing, stress-strain curves are obtained, resulting left shifted and with increased slope those of aneurysmal walls respect to those of non-aneurysmal walls, therefore the aneurysmal region turns out to be stiffer.

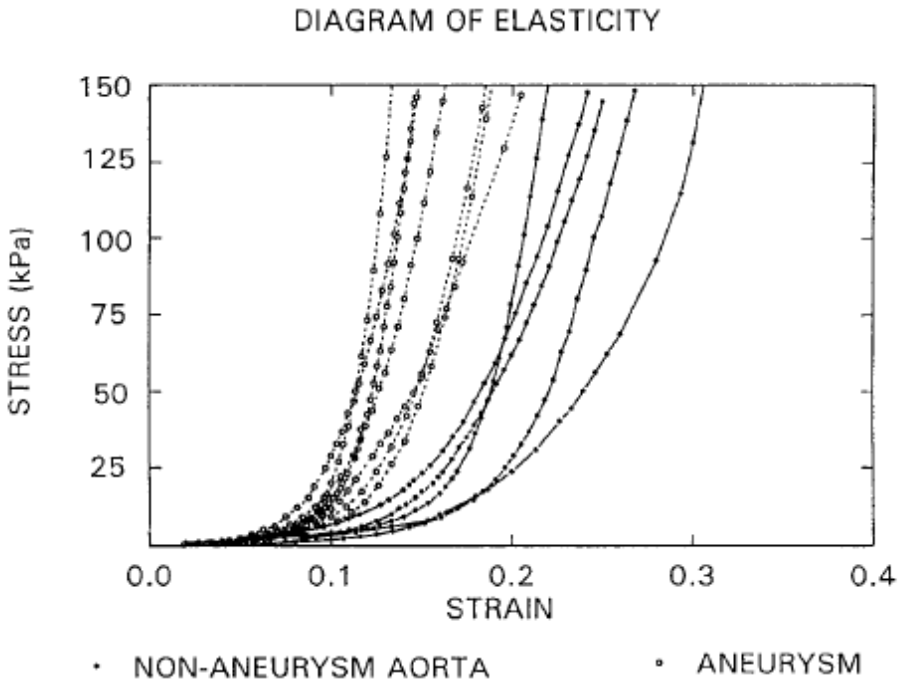

Figure 1.83: stress-strain curves [6]

Pathophysiology

The elastin degradation, associated to activity of specific proteases, inducts an inflammatory state that leads to a leucocyte and macrophages recruitment into the aortic wall; these inflammatory cells, that break into the media and adventitia, come from arterial blood and from medial neovascularization, common into abdominal aortic aneurysm[7]. Lymphocytes and macrophages produce cytokines that trigger the proteases activation. The proteolytic enzymes, responsible for elastin degradation, are part of matrix metalloproteinases (MMPs), excess MMPs degrade the structural proteins of the aortic wall, by allowing cells to infiltrate inside extracellular matrix. An autoimmune process plays a key role in the development of the abdominal aortic aneurysm.

Treatment Guidelines

Often AAA is an asymptomatic pathology, so people at risk should undergo screenings periodically; with symptomatic AAA, abdominal pain, back pain and embolic events can be noticed[8], in this latter case seems to be more high the risk of rupture of the vessel wall.

Just because the current repair techniques are not without complication[9], considering that the most are old patients, with comorbidities, surgeons must establish to intervene surgically only when the risk of rupture is higher than the risk of operative mortality. Exist, in fact, the guidelines that identify the AAA relevance, based on the AAA sizes; a diameter of 5.5 cm has be considered as a threshold[5], for AAA of diameters between 3 and 5.5 cm, patients are kept under surveillance with periodical screening, using ultrasonography, a safe, high sensitivity and specificity technology, for diameters upper to 5.5 cm the guidelines suggest to intervene surgically. These certain cut-off points represent mean values emerged by sever randomized trials, but they have to be considered as estimation of AAA risk of rupture, because they can be unreliable and misguided; indeed, autopsy studies detected that small AAAs can rupture while some larger, far above the surgical threshold, remain intact for a long time, time that exceeds the life expectancy of the

patients[9]. In view of this, some studies, based on computational patient-specific modelling, through CT scan data acquisitions, investigated the role of AAA shape on the risk of rupture, evaluating the wall stress, it results that asymmetry of the aneurysm geometry has certainly an impact.

Peak Wall Stress

Stress is a measure of the internal forces induced per unit area of the arterial wall due to the wall pressure and the flow[9]. The blood pressure, expanding the wall outwards, causes an in-plane wall stress that is the leading stress responsible for the wall deformation; instead, the flow produces shear stress that is orders of magnitude smaller than the wall stress, therefore it appears that only this latter affects the AAA biomechanical behaviour. The peak wall stress (PWS) is considered the maximum load that has to be sustained by the aortic wall during the maximum systolic pressure. Classical engineering stress analysis of simple axisymmetric shapes shows that the stress in hoop and longitudinal directions is directly proportional to the diameter, and inversely proportional to the thickness of the aneurysm wall[10]; in real aneurysms, more complicated asymmetric shapes are present, so the wall stress depends on entire geometry of the AAA, not only on diameter. Consequently, patient-specific AAA geometries, through the finite volume analysis method, with data acquired by computed tomography (CT) were evaluated to calculate wall stress distribution and PWS values[9]. The finite volume method works by dividing the geometry into a finite number of volumes which are connected together at their corners, called nodes, and as the number of volumes increases and the size of each individual volume decreases, the accuracy of the solution improves; it needs to choose a correct number of volumes in order to obtain a desirable accuracy. Manual extraction of the AAA geometry CT slices inevitably introduces several errors into the analysis, enhanced method for automated extraction of AAA external wall geometry should be used. Moreover, the thickness of the wall is difficult to calculate, it could also not be constant for all the aneurysm and, in addiction, biomechanical properties of the wall are assumed. The peak blood pressure is important to calculate the PWS, because it permits to evaluate if and where the peak wall stress exceeds the wall yield strength,

generating the AAA rupture, but the measurement of a patient's peak blood pressure is almost impossible. Even though the limits descripted above, PWS is suggested to be a better predictor of rupture than maximum AAA diameter[11].

In presence of rupture, there is a strong association between the site of the peak wall stress and the site of rupture[10]; high PWS has also been correlated with an increased growth rate of small AAAs[9].

The von-Mises stress can be used to evaluate the wall stress, it provides a single value of stress at any point calculated from the full 3D-stress tensor[10]. Wall stress distribution turns out to be non-homogeneous due to the difference in geometry at various points within an aneurysm.

1.3 Open Aneurysm Repair vs Endovascular Aortic Repair

For aneurysms with a diameter upper to 5.5 cm or symptomatic ones, surgery repair is recommended, nowadays two common practises exist: open air repair and endovascular aortic repair.

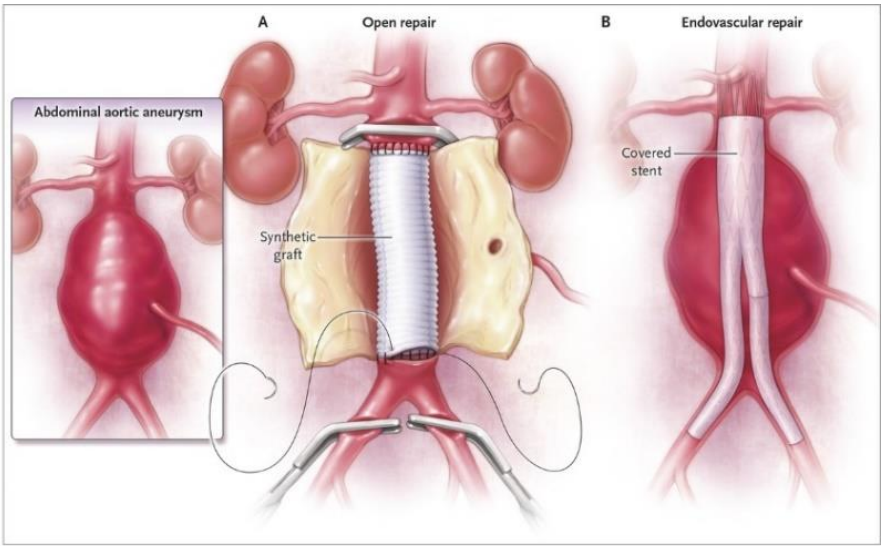

Figure 1.9: Open Repair vs Endovascular Repair

In open air surgery a large trans-peritoneal or retroperitoneal incision is made to expose the diseased section of the aorta, the aortic neck and iliac arteries are clamped to temporarily interrupt blood flow into the aneurysm[12] and then, the aneurysmal aorta is cut open and a synthetic fabric graft is placed to exclude the portion of dilated vessel from bloodstream, whereas in EVAR a stent graft, through the femoral artery, reaches the dilated area and there, in the right position, is expanded and attached to the aortic wall, it has the advantage to be a non-invasive technique. The endograft can be self-expanded or balloon-expanded, adhesion to the wall can be achieved through radial forces or hooks and barbs. The benefits of using hooks and barbs must be balanced against the risk of potential trauma to the aortic neck and adjacent structures, as do the risk of compromise the aortic neck by use the balloon-expanded.

Open air surgery is recommended for healthy people, without comorbidity, at low operatory risk, it seems to have, in fact, good long-term outcomes; it is also suggested for aneurysms with high growth rate.

For EVAR treatment, a pre-operatory imaging and pre-procedural planning is indispensable, it has to be evaluated the possibility to intervene through endovascular surgery, since anatomical characteristics may preclude its use. Aneurysm morphology much influences the endoprostheses positioning and release, it can represent a risk for distal embolism in presence of laminar thrombosis , it can be responsible for long-term failure of the device and it can prevent the total exclusion of the flow from the aneurysm sac.

Important features are the tortuosity and the angulation of the abdominal aneurysm, the characteristics of the aneurysmal neck, such as diameter, calcifications, thrombus presence and angulation, are crucial to decide if a patient is suitable for EVAR treatment, they may affect device migration. The aneurysmal neck, being the proximal junction of endoprostheses, has to guarantee secure attachment of the device. Morphology of iliac and common femoral arteries is fundamental to allow a vascular access to the endoprostheses, the vessel wall of iliac arteries is also the distal fixation area of device.

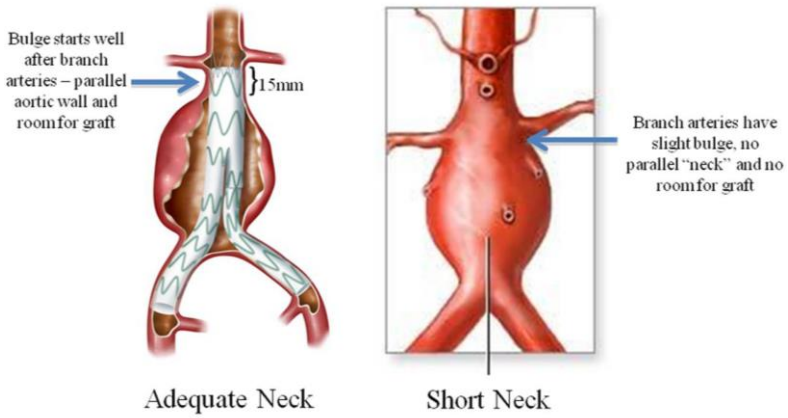

Figure 1.10: aneurysm neck for EVAR treatment

Endovascular aortic repair is preferable for elder people, which cannot sustain a heavy anaesthesia and an open repair surgery.

In patients with chronic renal insufficiency OAR and AVAR outcomes are been evaluated. Aortic aneurysm repair in this population has a higher mortality and morbidity rate than population with a normal renal function[13] The use of contrast in EVAR increases the risk to contract nephropathy with already impaired renal function, so many surgeons prefer to adopt open air surgery to avoid that, but the haemodynamic displacements, associated with OAR, are not positive for fragile renal function either. Subdividing patients based on severity degree of renal dysfunction, it results that for a moderate dysfunction at 30 days EVAR has significantly lower mortality, cardiovascular and pulmonary postoperative events. In patients with severe renal dysfunction complication rates are equally high for both OAR and EVAR.

In case of renal dysfunction, especially for severe ones, it is suggested to delay the surgery repair as much as possible, until the aneurysm diameter reaches to 5.5 or 6 cm, because the operative risks could outweigh the medical benefits in this patients population.

In case of ruptured abdominal aortic aneurysm, most of patients usually die before reaching the hospital, those survive are traditionally treated with emergent open aortic repair, but, after surgery, a high mortality rate is current anyway.

Endovascular aneurysm repair (EVAR) of non-ruptured abdominal aortic aneurysm (AAA) has greatly reduced the perioperative morbidity and mortality compared to open

surgery, however this benefit is not sustained in longer-term follow-up[14]. Moreover, endovascular stent-grafts are exposed to late several clinical complications and so, in some cases a reintervention is required. Long-term surveillance for these patients is needed and because of that, hospital costs for EVAR increase. There is no difference in the rates of stroke, myocardial infarction, or cardiac arrhythmia, which included atrial fibrillation, ventricular tachycardia, and ventricular fibrillation, at 30 days or in long-term follow-up[15].

Possible complications that can lead to reintervention are certainly endoleaks, they are identified by persistent blood flow in the aneurysm sac following endovascular aortic repair, therefore intrasaccular pressure remains elevated and so do the risk of rupture of the aneurysm[16]. They are usually classified in:

- Type I endoleaks: poor match between device and aortic wall is observed;
- Type II endoleaks: reverse flow into the aneurysm sac from aortic branches such as the inferior mesenteric artery or lumbar arteries is observed, it is the most common type;
- Type III endoleaks: it can be caused by fabric defect of the graft or by separation of the modular components;
- Type IV endoleaks: filtration of plasma through the graft is observed.

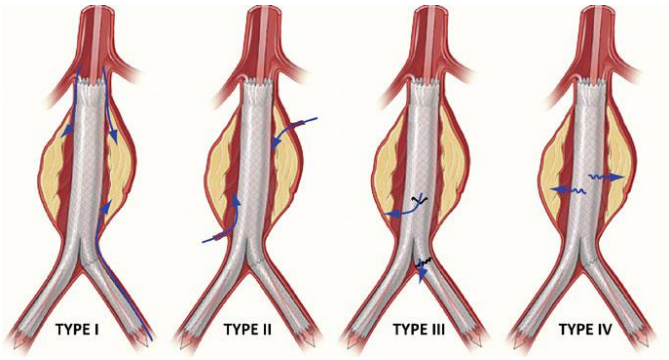

Figure 1.11: endoleak types [16]

Pulsatile blood flow and pressure are responsible for endograft migration, sometimes this latter is defined as a proximal or distal movement more than 5 mm or, in some case, 10 mm[16]. A more generic definition considers endograft movement as endograft migration if it results in an adverse clinical event, for which reintervention is needed. When the distal displacement forces exceed the strength of fixation at the

proximal and distal attachment zones endograft displacement is observed. The fixation force depends on the specific endograft fixation, the structural stiffness of the device, the portion of proximal and distal attachment zone and the severity of disease of the vessel wall in the landing areas.

1.4 Displacement forces

Even though EVAR devices have several advantages, some problems can occur especially concerning the long-term success. Displacement Forces can trigger endograft migration from implantation site, due to pressure forces, wall shear stress and weight forces acting throughout the cardiac cycle, they can lead to device failure. Displacement Forces, being the major cause of reintervention, are been greatly estimated by numerous studies, among which a study conducted by Mohan et al.[17] , where a theoretical model to calculate the displacement force was proposed; distal displacement force acting on the proximal fixation site is calculated for different pressures, diameters and angulations. An idealized bifurcated device is used to simulate haemodynamic forces acting on the graft. The fluid, flowing through the device, is divided into the two branches that represent the iliac limbs, both its direction and velocity vary due to the angle and to the changing diameter. For this model following assumptions are sustained: negligible fluid viscosity, so no fluid shear stress is present, symmetrical bifurcation in a horizontal plane, so the lateral forces and gravity forces are not considered, no pulsatile flow, so it can be seen as stationary problem.

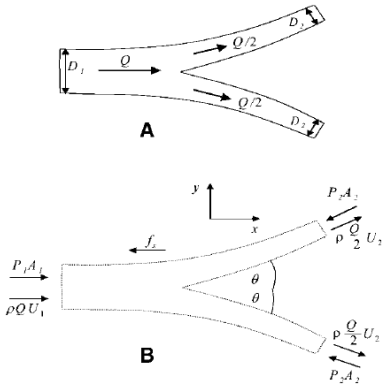

Figure 1.12: idealized bifurcated endograft [17]

Through the change in fluid momentum in the axial direction, acting forces along x can be evaluated:

$$P_1A_1 - 2P_2A_2\cos\theta - f_x = \rho Q(\frac{U_2}{2}\cos\theta + \frac{U_2}{2}\cos\theta - U_1)$$

where P_1, A_1, U_1 and P_2, A_2, U_2 are the pressure, the cross-sectional area and the velocity at the inlet and outlet respectively, ρ is the density of the fluid, Q is the volume flow rate and, finally, f_x is the axial component of the force exerted by the bifurcation on the fluid.
The right-hand side of the equation represents the rate of increase of the axial component of momentum.

P_2 is unknown so, from Bernoulli and continuity equation:

$$P_1 + \frac{\rho {U_1}^2}{2} = P_2 + \frac{\rho {U_2}^2}{2}$$

$$A_1U_1 = 2A_2U_2$$

f_x can be obtained:

$$f_x = P_1A_1 + \rho A_1{U_1}^2 - \rho\frac{{A_1}^2}{2A_2}{U_1}^2\cos\theta - 2A_2\cos\theta\,[P_1 + \rho\frac{{U_1}^2}{2}\left(1 - \frac{{A_1}^2}{4{A_2}^2}\right)]$$

From the third Newton's law, it can say that exists a force equal and contrary to f_x pushing the device distally, the displacement force.

In this study, diameter, pressure and angulation of the limbs were varied for each calculation while the other variables remained constant. It comes out that displacement force exerted at the proximal fixation site increases with high pressure, angulated iliac arteries, large proximal graft diameter and the degree of diameter change along the endograft; there is a linear relation between axial force and both blood pressure and proximal diameter, and a nonlinear relation between axial force and iliac limb angulation. Among the demographic and clinical variables, only current smoking and hypertension have an influence on graft migration. The displacement force, estimated with this model, has to be considered rough estimate because of all the assumptions took account above.

To avoid the problem of the aneurysm morphology in the EVAR procedure, customised endograft, known as Fenestrated Stent Graft (FSG), can be used, in a research performed by Kandail et al.[18], patient-specific analysis of displacement forces, acting on it, were examined for six patients; pre and post-operative patient geometry was reconstructed through computed tomography images.

To estimate displacement forces and the pulsatile blood flow, some assumptions were made:

- Continuity Equation ($u_{i,i} = 0$), Momentum Equation ($\rho\left(\frac{\partial u_i}{\partial t} + u_j u_{i,j}\right) = -p_i + \tau_{ij,j}$) and Stress Tensor ($\tau_{ij} = \eta\dot{\gamma}_{ij}$), where u_i is the velocity vector, p is the pressure scalar, ρ is the blood density that was chosen equal to 1060 kg/m^3, τ_{ij} is the shear stress tensor and $\dot{\gamma}_{ij}$ is the shear rate tensor;
- Non-Newtonian blood behaviour was adopted, whereby the apparent viscosity is:
  $\eta = \frac{\mu_p}{[1-\frac{1}{2}(k_0+k_\infty(\sqrt{\dot{\gamma}/\dot{\gamma}_c})/(1+\sqrt{\dot{\gamma}/\gamma_c})\Psi]^2}$,
  where μ_p is the viscosity of the blood plasma, Ψ is the haematocrit, $\dot{\gamma}/\dot{\gamma}_c$ is the relative shear rate;
- Womersley velocity profile at the inlet was imposed.

This displacement forces were evaluated by taking an area integral of the net pressure and WSS over the entire wall of the FSG in x, y and z directions:

$$F_{d,i} = \int_{A,i} pdA + \int_{A,i} (-\eta_w \frac{\partial u_t}{\partial n}|_{n=0})\, dA$$

Where the first integral is the force contribute due to the pressure and the second one is the force contribute due to the Wall Shear Stress.

The resultant displacement force is:

$$|F_d| = \sqrt{(F_{d,x})^2 + (F_{d,y})^2 + (F_{d,z})^2}$$

and de direction cosines:

$\theta_\alpha = \cos^{-1}\left(\frac{F_{d,x}}{|F_d|}\right)$, $\theta_\beta = \cos^{-1}\left(\frac{F_{d,y}}{|F_d|}\right)$, $\theta_\gamma = \cos^{-1}\left(\frac{F_{d,z}}{|F_d|}\right)$,

these are the angles relative to x, y, z axis.

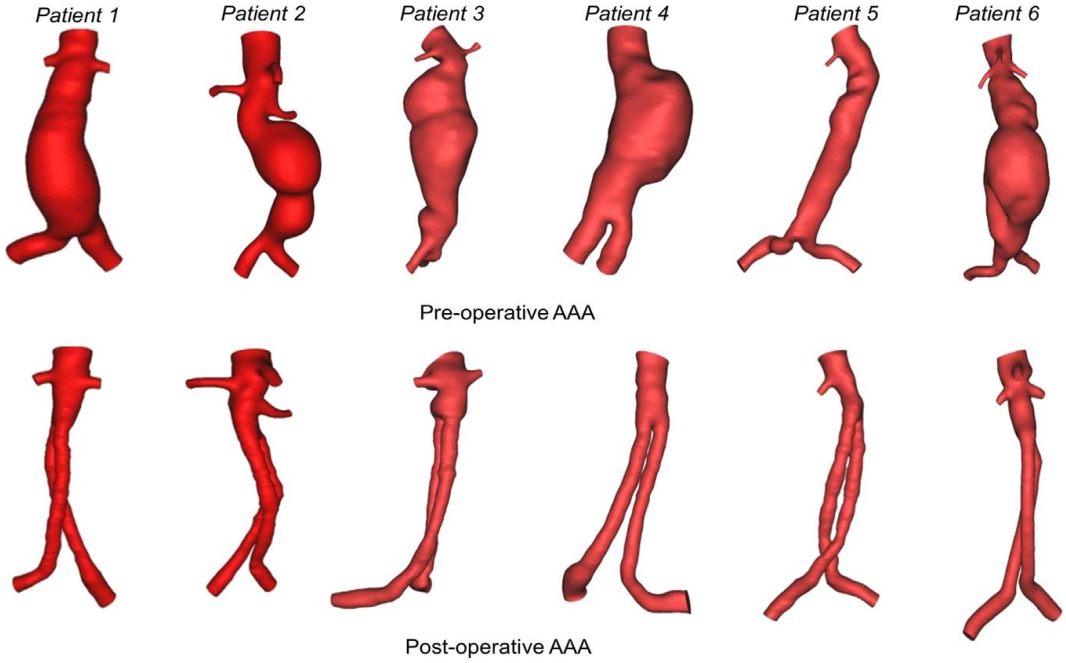

Figure 1.18: Patient-specific AAA models[18]

The cross-section area, the lateral neck angles and the antero-posterior neck angles were the parameters taking in account to evaluate the resultant displacement forces, the direction of these latter, in fact, strongly depends on the abdominal aortic aneurysm morphology and tortuosity; it resulted that direction of the displacement force did not vary during a cardiac cycle.

The magnitude of the force is generally influenced by the loads exerted by the pulsatile blood flow. It was found that there are significant individual variations in both magnitude and direction of the displacement forces on FSG, indeed, the peak displacement forces ranged from 1.9 to 14.3 N, whereas the mean value vary between 1.6–12.0 N. It was also discovered that the WSS component accounted for less than 1% of the displacement force, that it means pressure is the prevalent contributor of the overall displacement force.

Another study carried out by Figueroa et al.[16,19] investigated the impact of the curvature on the displacement forces exerted on the endografts. These displacement forces were calculated for patient-specific geometries of aortic endografts underwent realistic haemodynamic condition by means of Computational Fluid Dynamics (CFD). Endograft models were extracted from automatic segmentation of images derived by patient phase-contrast magnetic resonance angiography (MRA), subsequently, models

are discretized in an appropriate grid size. Womersley velocity profile is imposed on the inlet of the endograft model and, subsequently, CFD analysis is performed whereby the Navier–Stokes equations of an incompressible fluid are solved in the domain of interest, blood flow velocity and pressure are calculated in order to understand how they act on the endograft and how they affect its stability. Magnitude and direction of displacement forces were quantified by integrating the sum of the wall shear stress and the normal stress over the endograft surface, important antero-posterior and lateral components of the force were found; the downward component of the force in the direction of blood flow, F_z, was small compared to the sideways component, F_y. In line with other study, it appeared that pressure provides predominant contribution to the displacement force and because of that, hypertension should be kept under control constantly. Furthermore, this patient-specific model was modified in order to obtain an almost flat or planar configuration without changing the dimensions of the device, so curvature in the antero-posterior and lateral directions in the aneurysm zone was reduced. The curvature of the endograft is expressed by the formula C=1/R, where R is the radius that approximately fits a circle through the path of the graft. The curvature of the endograft is related to some extent to the neck and iliac angulations, but it is also determined by the level of tortuosity of the aneurysm sac.

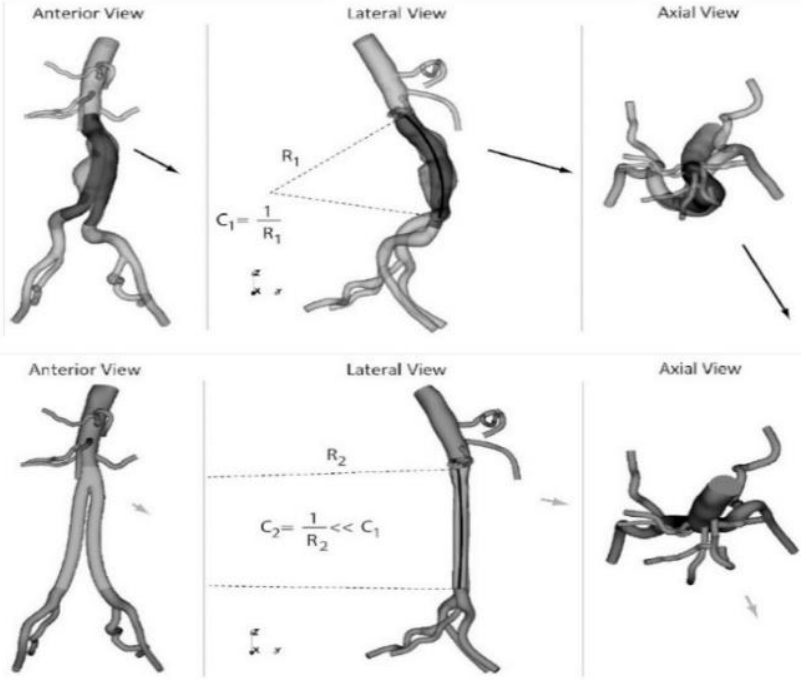

Figure 1.13: curved endograft and modified endograft [19]

The primary direction of displacement force appeared to be always sideways with respect to the direction of blood flow. Reducing the neck angulation, a decrease by 17% of the displacement force as compared to the normal curved model is noticed, as well as reducing iliac angulation produces a decrease by 58% of total displacement force compared to the normal curved model.
The temporal average of the total displacement force on this new model was observed to be decreased more than five-fold compared to the total displacement force on the curved endograft, values of 0.8 N and 5 N, respectively, were identified. It is evident that the total displacement force growths as the curvature increases, particularly in the sideways direction, whereby, even though, generally, endograft migration is clinically regarded as longitudinal or caudal migration, lateral movement of endografts within the aneurysm sac could be potentially seen as a predictor of stent-graft instability.

1.5 Viscous Dissipation Rate

During a fluid dynamics simulation, the viscous dissipation rate (VDR) is an indicator used to determine the amount of mechanical energy irreversibly converted into internal energy, heating up the fluid. Knowing the amount of energy dissipated during the cardiac cycle it could be an important factor because more energy it is dissipated more is the work requests from the heart to pump the blood to the periphery of the body. Dissipation is higher in regions with important velocity gradients and in presence of elevated turbulent flow. It is been already used to calculate the power loss in a Fontan connection study[20]. In this thesis work, it will be exploited to evaluate the flow efficiency losses in the stent devices and to investigate a possible relation between the VDR and the displacement forces, DFs that acting on the stents, under certain conditions, may lead to failure of the endograft.

Chapter 2

Methods and Analysis

In this Chapter a generic handling of the discussed topics is conducted.

In the first part, the data-set of this master thesis is presented and Computational Fluid Dynamics principles are explained.

In the second part, all significative treating parameters are described as follows: Viscous Dissipation Rate, Displacement Forces, Geometric Indexes and Bulk Flow Indexes.

2.1 3D Models

Ten male patients, with age=68.6±8.6 years, affected by AAA and treated with EVAR, at the University Hospital of Ioannina (Ioannina, Greece), are taking account in this master thesis work.

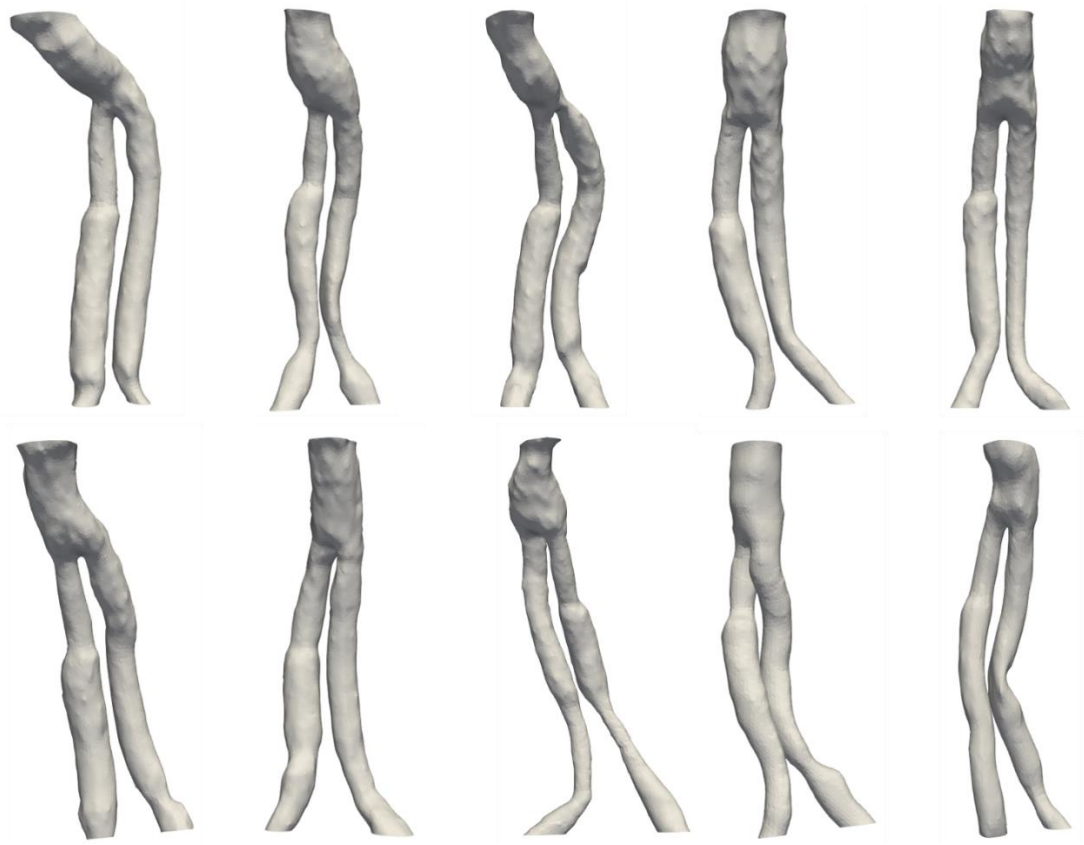

Figure 2.1: ten patients' specific post-EVAR models

A commercial endovascular device, the Gore Medical Excluder®, (W.L. Gore & Associates, Flagstaff, AZ)[21], was used for this data-set, it is a self-expanding nitinol stent, a shape memory titanium-nickel based alloy with ePTFE and FEP fabric; stent-grafts were all fixed at the same landing zones, with the same method of attachment. Models were obtained from clinical images captured one month after implantation through computer tomography angiography (CTA) scans. 2D DICOM images were segmented and a 3D geometry was extracted by means of MIMICS software, looking upon the device surface, excluding the stent wall thickness and the aneurysmal vessel. Following the morphologic profile of the centerline, models were subdivided in three different parts, the body, just

above the centerline bifurcation, and the branches, left and right, starting from the point in which centerline splits.

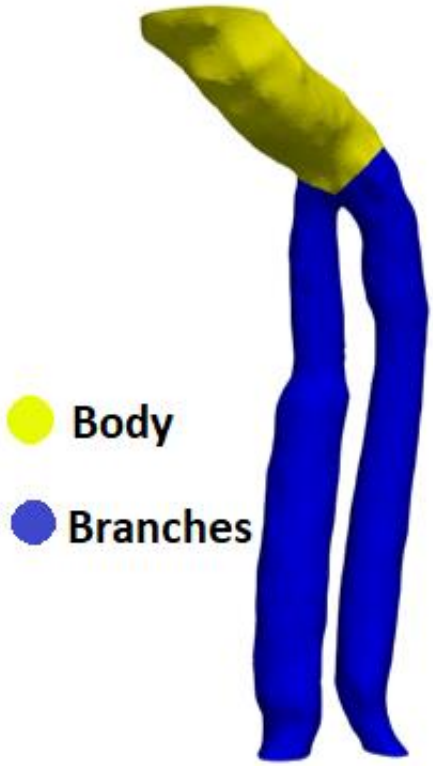

Figure 2.14: Geometric Segments of a treated model

2.2 Computational Fluid Dynamics

The Fluid Dynamics analysis was performed using the CFD solver ANSYS Fluent® based on the finite volume methods, it allows to evaluate hemodynamic, the fluid flow behaviour, inside the domain of interest and its effect on the vessel walls; high spatial and temporal resolutions can be reached.

Through the CFD, two fundamental equations, that govern fluids, for a 3D domain can be approximately solved: conservation of mass and conservation of momentum. Estimated solutions are due to the transformation of integral-differential equations into algebraic equations, necessary for computational application; better approximations are obtained with the increase in number of mesh volumes.

The conservation of mass equation is:

$$\frac{\partial \rho}{\partial t} + \nabla \cdot (\rho \vec{V}) = 0$$

The conservation of momentum is:

$$\rho \frac{\partial \vec{V}}{\partial t} + \rho(\vec{V} \cdot \nabla)\vec{V} = -\nabla p + \rho \vec{g} + \nabla \cdot \tau_{ij}$$

Where the inertial term, on the left side of the equation, is balanced by pressure forces, viscous forces and field forces.

The behaviour of Newtonian incompressible fluids is described by the following equation:

$$\begin{cases} \tau = \mu \dfrac{\partial v}{\partial t} \\ \rho = constant \end{cases}$$

So, the conservation of mass and momentum equations become:

$$\begin{cases} \nabla \cdot \vec{V} = 0 \\ \rho \left(\dfrac{\partial \vec{V}}{\partial t} + \vec{V} \cdot \nabla \vec{V} \right) = -\nabla p + \rho \vec{g} + \mu \nabla^2 \vec{V} \end{cases}$$

They can be analytically determined only in simple cases, but in most of fluid dynamic problems, for biomedical applications, approximated solutions are obtained; numerical methods were applied, so simplifications of the conservation laws were accepted. Models were discretized following the finite volume method, so, examining each mesh volume as a single control volume, conservation equations were solved in. Algebraic equations were iteratively calculated and convergence criteria was chosen to identify the solutions. Residuals, for continuity and velocity components along x y and z directions, were imposed equal to 10^{-4} to provide good convergence, so accuracy, of the solution for each time step. Solution convergence is obtained when the difference between an iteration and the previous one is less than a key value:

$$\frac{x_{k+1} - x_k}{x_k} < \epsilon$$

Where x_{k+1} and x_k are the variable values at the k+1-th and k-th iterations respectively, whereas ϵ is the user-defined limit value.

After a sensitivity analysis, performed in a previous study, for the ten models considered in this master thesis a tetrahedral radial mesh was used because steeper velocity variations close to the wall were found, compared to the bulk.

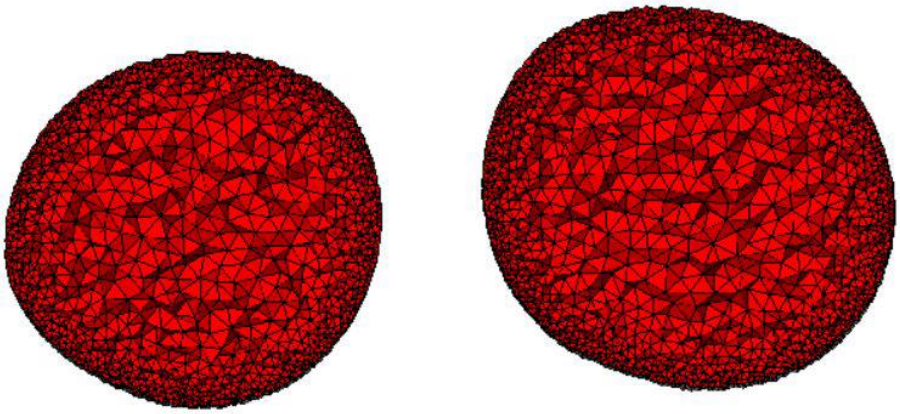

Figure 2.3: computed mesh

2.2.1 Boundary Conditions

To perform simulations and investigate the hemodynamic parameters, some boundary conditions and assumptions were considered.

For models of AAA treated with EVAR, belonging the major arteries, blood was assumed as Newtonian and incompressible fluid.

Imposed parameters:

- density: ρ=1050 $\frac{Kg}{m^3}$
- dynamic viscosity $\mu = 3.5 \cdot 10^{-3}\ Pa \cdot s$
- rigid wall, with no slip condition
- inflow and outflow boundaries

From literature, time dependent pressure waveform, as Neumann condition, was applied at the inflow boundary, whereas flow rate waveforms, scaled depending on the exit areas, were imposed at the outflows[21-22].

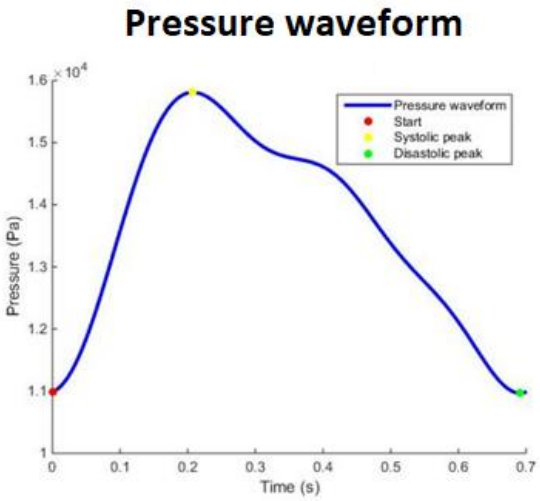

Figure 2.4: inflow boundary condition

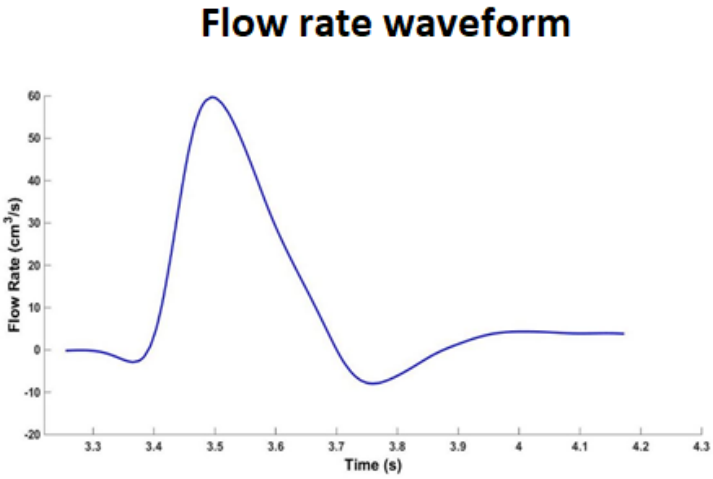

Figure 2.5: outflow boundary condition

Unsteady simulation was implemented, and two cardiac cycles were performed to extinguish the transitory. The cardiac cycle period (T) was set of 0.7 s and time steps amplitude (Δt) was chosen of 0.0035s.

2.3 Viscous Dissipation Rate

The viscous dissipation rate, recognised as hemodynamic metric, can be derived from differential energy conservation analysis, following the first thermodynamic law, under which time rate of internal energy variation of a system is equal to the sum of the time rate of transfer heat and the time rate of work done. It results that the differential power lost can be described as[20]:

$$\dot{e}_{loss} = -p\left(\nabla \cdot \vec{U}\right) + \underline{\tau} : \nabla\vec{U}$$

Assuming to manage with a Newtonian fluid, the earlier equation becomes:

$$\dot{e}_{loss} = -p\left(\frac{\partial u_x}{\partial x} + \frac{\partial u_y}{\partial y} + \frac{\partial u_z}{\partial z}\right) + \mu\left[\begin{array}{c} 2\left(\frac{\partial u_x}{\partial x}\right)^2 + 2\left(\frac{\partial u_y}{\partial y}\right)^2 + 2\left(\frac{\partial u_z}{\partial z}\right)^2 + \left(\frac{\partial u_x}{\partial y} + \frac{\partial u_y}{\partial x}\right)^2 + \\ + \left(\frac{\partial u_x}{\partial z} + \frac{\partial u_z}{\partial x}\right)^2 + \left(\frac{\partial u_y}{\partial z} + \frac{\partial u_z}{\partial y}\right)^2 - \frac{2}{3}\,\mu\left(\frac{\partial u_x}{\partial x} + \frac{\partial u_y}{\partial y} + \frac{\partial u_z}{\partial z}\right)^2 \end{array}\right]$$

Where p is the static pressure, u_x u_y and u_z are the components of the velocity vector and μ is the dynamic viscosity.

Subsequently, if the fluid is also incompressible, then:

$$VDR = \mu\left[2\left(\frac{\partial u_x}{\partial x}\right)^2 + 2\left(\frac{\partial u_y}{\partial y}\right)^2 + 2\left(\frac{\partial u_z}{\partial z}\right)^2 + \left(\frac{\partial u_x}{\partial y} + \frac{\partial u_y}{\partial x}\right)^2 + \left(\frac{\partial u_x}{\partial z} + \frac{\partial u_z}{\partial x}\right)^2 + \left(\frac{\partial u_y}{\partial z} + \frac{\partial u_z}{\partial y}\right)^2\right]$$

VDR has to be integrated over the entire domain volume to be identified as the general power loss from the control volume:

$$\Phi = \mu\int_V\left[2\left(\frac{\partial u_x}{\partial x}\right)^2 + 2\left(\frac{\partial u_y}{\partial y}\right)^2 + 2\left(\frac{\partial u_z}{\partial z}\right)^2 + \left(\frac{\partial u_x}{\partial y} + \frac{\partial u_y}{\partial x}\right)^2 + \left(\frac{\partial u_x}{\partial z} + \frac{\partial u_z}{\partial x}\right)^2 + \left(\frac{\partial u_y}{\partial z} + \frac{\partial u_z}{\partial y}\right)^2\right]dV$$

Φ, being a power loss, is measured in Watt.

Furthermore, in this study power loss was integrated on time, to evaluate the energy lost during all cycle and during its main phases, systole and diastole.

$$E_{lost} = \mu\int_T\int_V\left[2\left(\frac{\partial u_x}{\partial x}\right)^2 + 2\left(\frac{\partial u_y}{\partial y}\right)^2 + 2\left(\frac{\partial u_z}{\partial z}\right)^2 + \left(\frac{\partial u_x}{\partial y} + \frac{\partial u_y}{\partial x}\right)^2 + \left(\frac{\partial u_x}{\partial z} + \frac{\partial u_z}{\partial x}\right)^2 + \left(\frac{\partial u_y}{\partial z} + \frac{\partial u_z}{\partial y}\right)^2\right]dV\,dt$$

2.4 Displacement Forces

Displacement forces exerted by blood flow on implanted device walls are defined as the sum of pressure forces, friction forces and weight force. In this study all the simulations were performed with no gravity, so the weight contribution was neglected. For each time step, DFs can be calculated as:

$$DF(t) = \int_S p\,\mathbf{n}\,dS + \int_S \boldsymbol{\tau_w} dS$$

Where p is the net pressure, $\mathbf{n}$ is the locally normal vector to the domain wall, τ_w is the WSS vector and S is the surface area of the endograft on which forces acting. DFs can be evaluated separately through body and branches, moreover, it is significant to estimate the mean DF, the axial DF and the perpendicular DF. The mean DF was defined as:

$$DF_{mean} = \frac{1}{T}\int_T DF(t)\,dt$$

Where T can represent the entire cycle period, but also systole and diastole periods.

The DF vector was calculated on the centre of gravity for each segment of the model, it can be broken down into two components, one axial and another perpendicular. The axial DF is determined as the DF projection on the nearest centerline point, along the centerline direction in that point. Therefore, the perpendicular DF is consequently given as the perpendicular vector to the axial one.

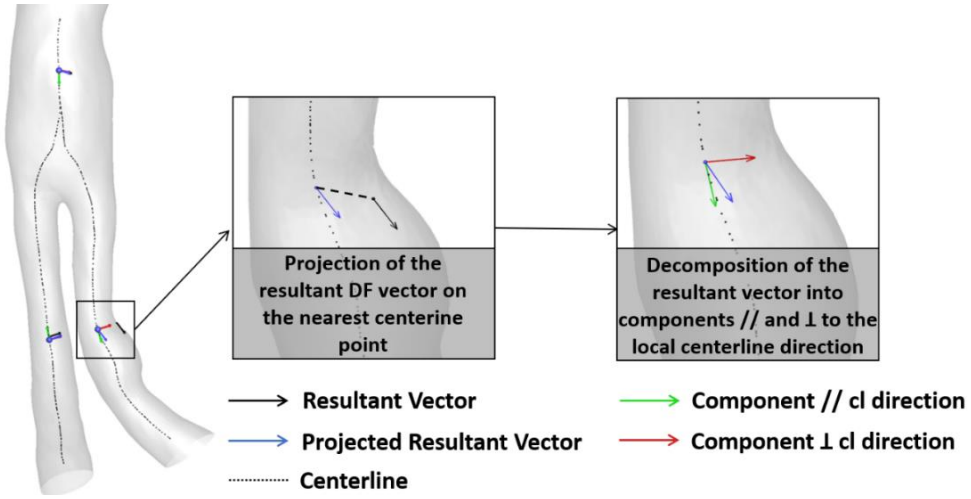

Figure 2.6: Displacement Force vectors

2.5 Geometric Indexes

It well knows that the geometry of the domain has an impact on the hemodynamics, so it is remarkable to investigate some geometric features.

2.5.1 Curvature and Torsion

Curvature and Torsion are the main characterizing parameters the centerline, they provide description of parametrized curve in 3D; curvature gives idea about how deviates curve from to be a straight line on a plane. From VMTK, discretized centerline is given but, to compute curvature and torsion, an analytical continuous form is request, it was obtained through the method based on free-knots regression spline. Knots number and their positions was not selected in advance, they are chosen on the basis of minimization of the penalized average squared error criterion. An order of the free-knots regression spline was identified so that derivatives, up to fourth order, of the computed continuous centerline were guaranteed without discontinuities. Curvature and Torsion are estimated as following[21]:

$$\kappa(s) = \frac{|\boldsymbol{C}'(s) \times \boldsymbol{C}''(s)|}{|\boldsymbol{C}'(s)|^3}$$

$$\tau(s) = \frac{[\boldsymbol{C}'(s) \times \boldsymbol{C}''(s)] \cdot \boldsymbol{C}'''(s)}{|\boldsymbol{C}'(s) \times \boldsymbol{C}''(s)|^2}$$

Where $\boldsymbol{C}$ is the curve representing the centerline, s is the curvilinear abscissa, $\boldsymbol{C}'(s)$, $\boldsymbol{C}''(s)$ and $\boldsymbol{C}'''(s)$ are first, second and third derivatives of $\boldsymbol{C}$ with respect to s, respectively.

2.5.2 Cross-Sectional Area and variation Rate

In VMTK the centerline is computed as the place of the points corresponding to centers of maximal inscribed spheres through the domain, knowing that the cross-sectional area A(s) is easily defined as:

$$A(s) = \pi R(s)^2$$

Whereas, the variation rate of the cross-sectional area coincides with the first derivative of A(s) with respect to the curvilinear abscissa:

$$R(s) = \frac{dA(s)}{ds}$$

Considering a vascular segment of a non-specific length L, mean value of one of this geometric index (GI) is calculated as[23]:

$$GI_{mean} = \frac{1}{L}\int_0^L GI(s)ds$$

Maximum and Peak-to-Peak values for the geometric quantitative descriptor were also considered, where Peak-to-Peak value is calculated as the maximum minus minimum of the parameter in question.

2.6 Bulk Flow Indexes

Bulk Flow descriptors characterize the helical flow structures of the fluid dynamics domain, these latter, being responsible for mass transfer, have probably an impact on hemodynamics and they could affect blood-vessel wall interaction; for this reason, helicity is measured.

Helicity is a scalar that identify alignment of velocity and vorticity vectors:

$$h(\boldsymbol{s};t) = \boldsymbol{V}\cdot\ (\nabla\times\boldsymbol{V}) = \boldsymbol{V}(\boldsymbol{s};t)\cdot\boldsymbol{\omega}(\boldsymbol{s};t)$$

The vorticity represents the spin rotation of the streamlines of the fluid domain.

Bulk flow indexes of interest are:

- Mean Helicity h_1, it provides measure of how contra-rotating structures are balanced:

$$h_1 = \frac{1}{TV_i}\int_T \int_{V_i} \boldsymbol{V}(\boldsymbol{x},t)\cdot\boldsymbol{\omega}(\boldsymbol{x},t)\,dVdt$$

  If h_1=0 →structures do not rotate, or structures are balanced;

- Helicity intensity h_2, it gives an idea of rotation of the structures inside domain, it assumes always positive values:

$$h_2 = \frac{1}{TV_i}\int_T \int_{V_i} |\boldsymbol{V}(\boldsymbol{x},t)\cdot\boldsymbol{\omega}(\boldsymbol{x},t)|\,dVdt$$

  If h_2=0 →structures do not rotate, if h_2>0 →structures rotate, high values of h_2 identify a lower risk of exposure to potentially atherogenic wall shear stress;

- h_3, it varies between -1 and 1, the value sign determines what rotation type prevails:

$$h_3 = \frac{h_1}{h_2}$$

- h_4, it says how unbalanced the structures are:

$$h_4 = \frac{|h_1|}{h_2}$$

It important to evaluate the spiral-shape motion through the cardiac cycle, because it reduces recirculation regions that promote thrombus formation.

2.7 Statistical Analysis

Statistical analysis was performed to investigate a possible correlation between the Viscous Dissipation Rate and the other characterizing parameters descripted above, considering the entire model or body and branches separately, during systole, diastole or all cycle.

A preliminary valuation was conducted to figure out if the two considered samples are normally distributed by means of Shapiro-Wilk test[25].

The W test statistic is determined as:

$$W = \frac{(\sum_{i=1}^{n} a_i y_i)^2}{\sum_{i=1}^{n}(y_i - \bar{y})^2}$$

Where y_i is the i-th component of the ordered random observations vector and $\{a_i\}$ are the normalized 'best linear unbiased' coefficients tabulated in Sharan & Greenberg.

Normality distribution verification comes from a comparison between two alternative estimators of the variance σ^2:

~ Non-parametric estimator, in which mathematical models don't need a priori hypothesis on population characteristics, based on optimal linear combination of order statistic of the random variable in the numerator;

~ Parametric estimator, which is the sample variance, in the denominator.

If the sample coming from a normal population, then the two different estimators represent, up to a constant, the same quantity; that is no true for non-normal population.

If at least one of two samples turns out to be non-normally distributed, then Spearman test is employed, Pearson test otherwise. Pearson test investigates a possible linear relation between variables, whereas Spearman test verifies a potential monotonic relation; both tests provide as outcomes:

- statistic index P-value, if it is < 0.05, the relation can be defined statistically significant;
- correlation coefficient ρ, it varies from -1 to 1 and gives a correlation measure, for the Pearson relation it is computed as:

$$\rho_{XY} = \frac{\sigma_{XY}}{\sigma_X \sigma_Y}$$

Where X and Y are the variables to compare, whereas for Spearman relation values turn into ranks, so:

$$\rho_S = \frac{\sum_i (r_i - \bar{r})(s_i - \bar{s})}{\sqrt{\sum_i (r_i - \bar{r})^2} \sqrt{\sum_i (s_i - \bar{s})^2}}$$

Where r_i and s_i are respectively the rank values of the first and second variable for the i-th observation.

When correlations were estimated between variables in branches, since the two are seen as together, Wilcoxon-Mann-Whitney test was been needed to carry out. It is a non-parametric test, it is effective for both normal and non-normal distributions and it is used to detect if statistical samples belong to the same population. Let suppose that x and y be random variables having continuous cumulative distribution functions f and g, respectively, the null hypothesis of the test is that the two samples have been derived from the same population, in other words $f = g$[26]; the alternative is that the variable x is stochastically smaller than y if $f(a) > g(a)$, for every a.

Correlation results are reported subsequently.

Chapter 3

Results and Discussion

Intention of this chapter is to present results obtained from this master thesis work and subsequently to discuss them.

The first part refers to the Viscous Dissipation Rate, evaluating it in several regions of the model through the entire cardiac cycle, but also in systole and diastole, then, in the same way, the Displacement Forces are examined.

Secondly, outcomes derive from statistical analysis are reported.

3.1 Post-processing Results: Viscous Dissipation Rate

The viscous dissipation rate is the main parameter analysed in this study, it is evaluated in several condition and different regions of implanted stent-grafts. For each patient, for each time step, the VDR, integrated on the entire domain, was calculated, then statistical analysis was performed on data set, so the mean value and the standard deviation of power losses during cardiac cycle were estimated for the entire model, but also for the body and branches regions.

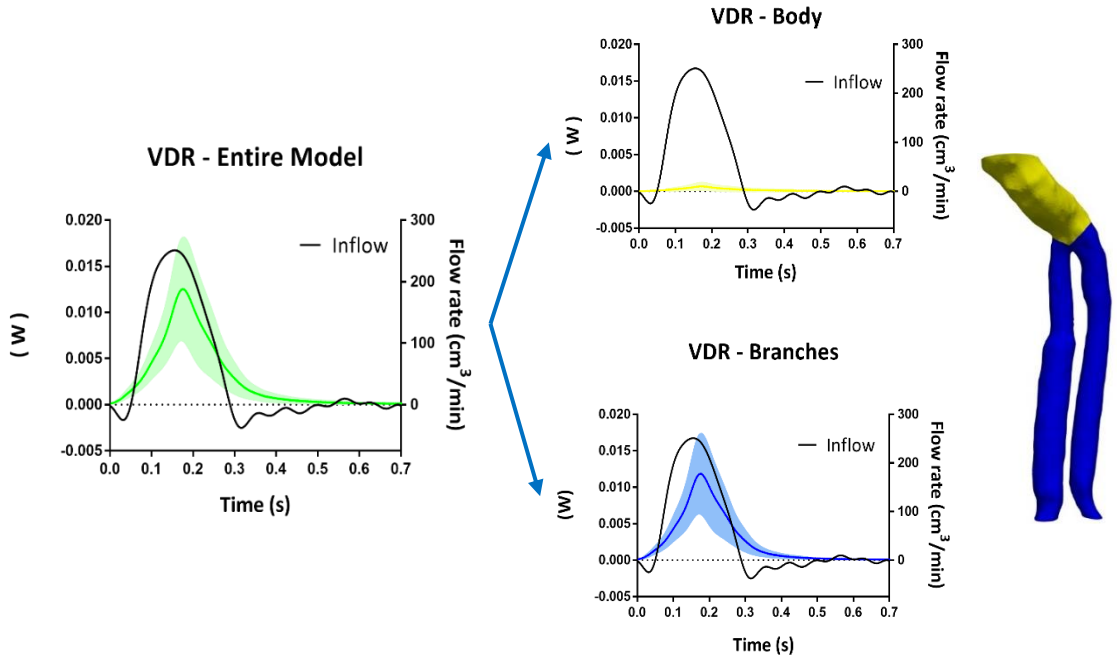

Figure 3.15: power loss during a cardiac cycle

For each patient, the Viscous Dissipation Rate was integrated on volume and on systole, on diastole and on all the cycle, so energy loss was computed and on data-set statistical analysis was performed, from which mean values and standard deviations were pulled:

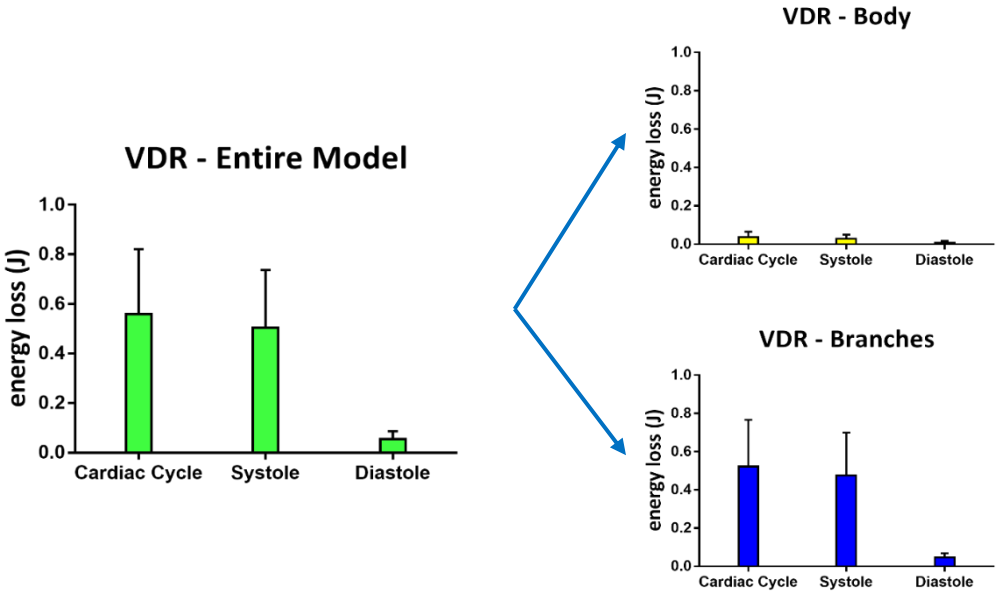

Figure 3.16: energy lost, mean and SD

Mean values of energy loss through all models are equal to 0.558±0.249 J on all the cardiac cycle, 0.504±0.222 J on systole and 0.054±0.030 J on diastole.

From figure 3.1 and 3.2, it clearly results that power losses are predominant during the systole, furthermore the most significant contribution derives from branches, indeed, it can be noted as the bar-graphs deriving from the branches and from the entire model are more similar compared to the bar-graph arising from the body in terms of order of magnitude.

Viscous Dissipation Rate Colormaps

Viscous Dissipation Rate integrated on total domain was examined. In order to identify geometrically the regions more affected by energy loss, evenly through the 10 patients, iso-surfaces and cross-sectional cut-planes of 90th percentile equal to $4.6e^{-7}$ J calculated for the entire cycle are illustrated below, respectively, on the cardiac cycle, systole and diastole; same threshold was applied to be able to compare the three distinctive events.

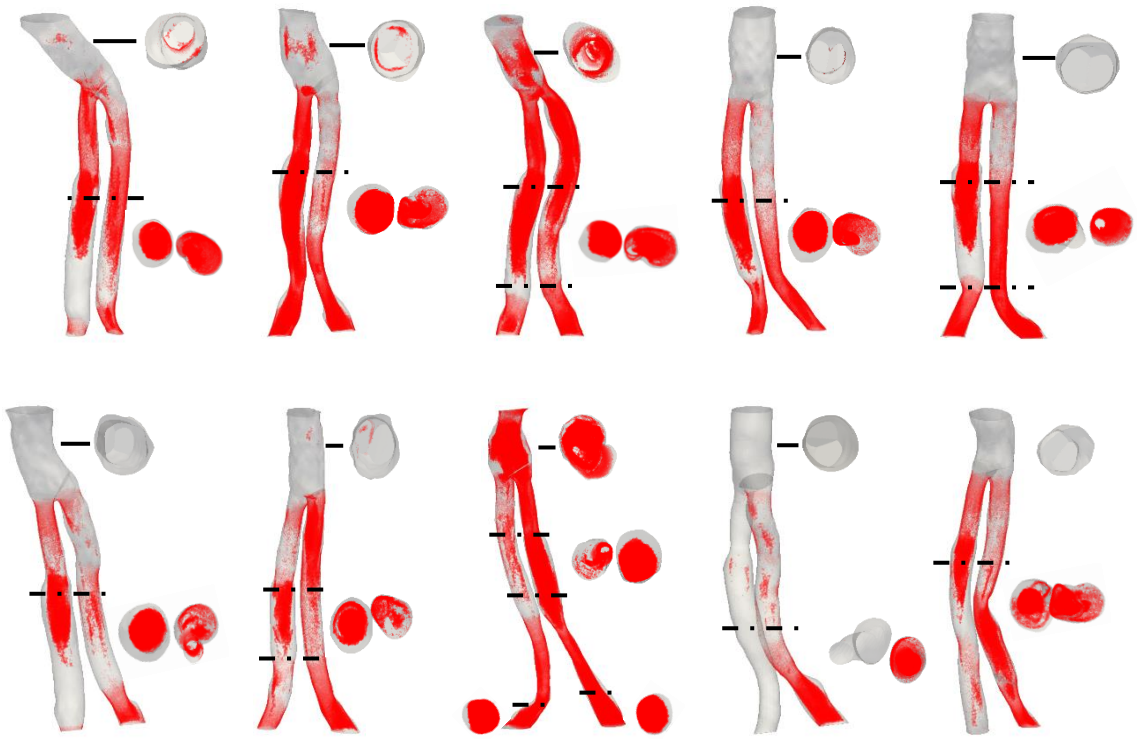

Figure 3.17: energy lost in Excluder models on the cardiac cycle

It can be noticed that, as expected, after a cardiac cycle, zones more inclined to energy loss appear to be the branches, particularly in the central regions, whereas in the body, where it is present, the regions affected by energy loss are distributed along the vessel wall.

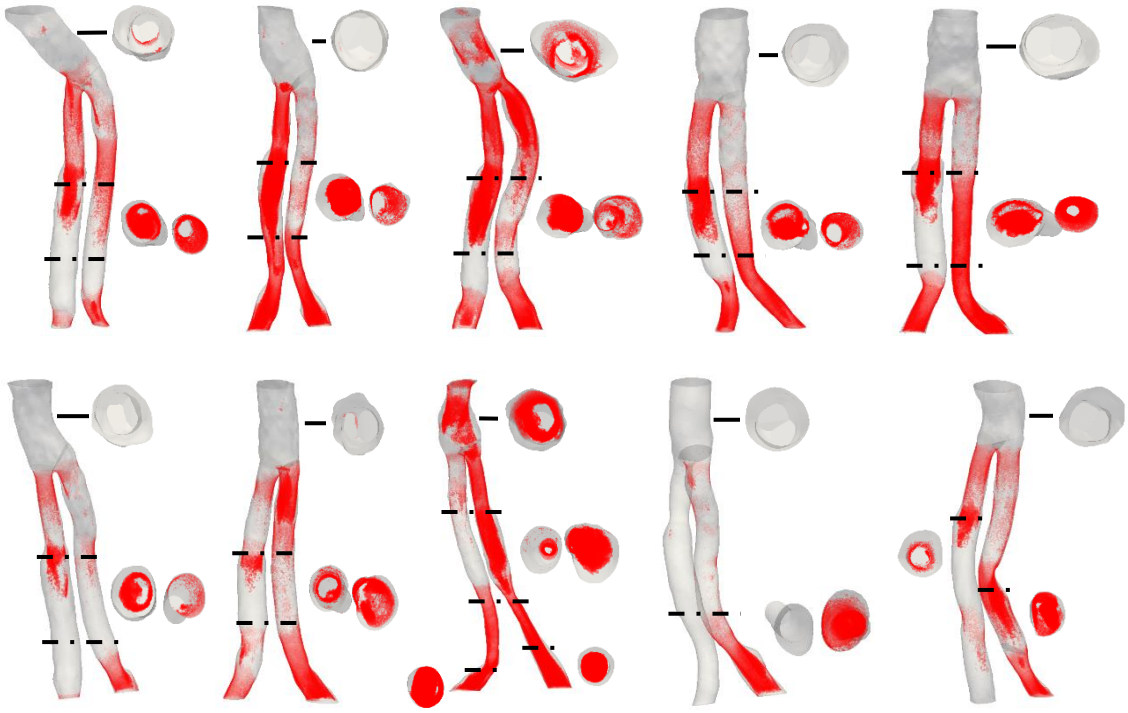

Figure 3.4: energy lost in Excluder models on the systole

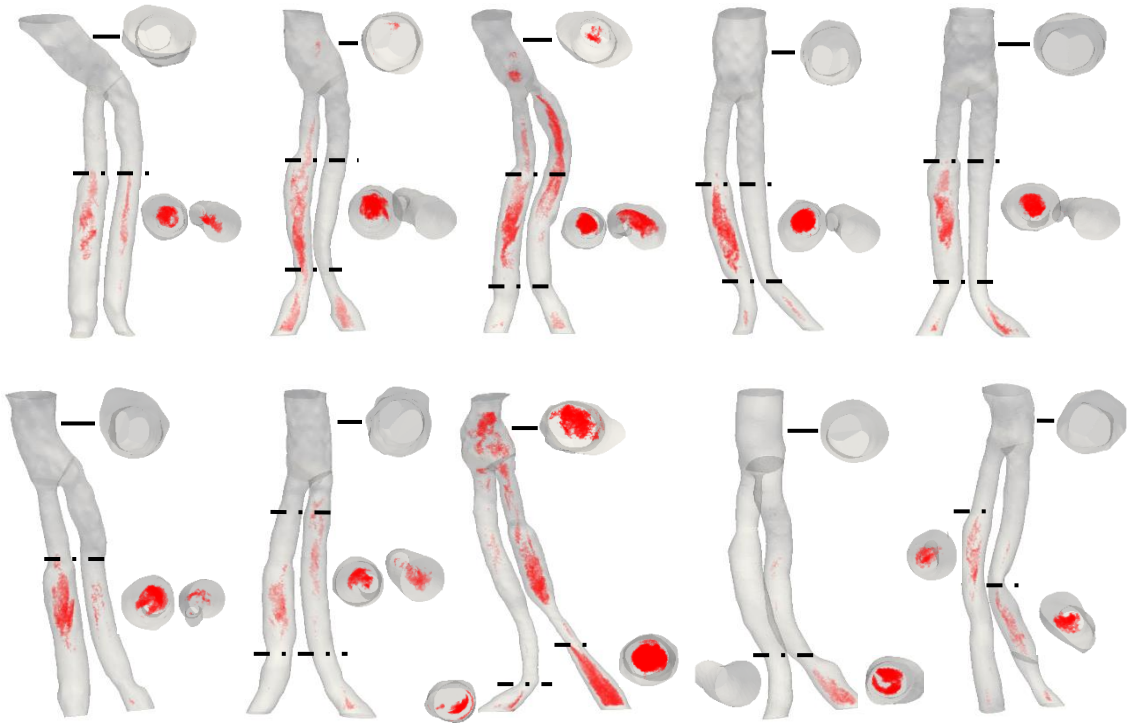

Figure 3.5: energy lost in Excluder models on the diastole

Comparing the two last images, it evident appears that regions more incline to energy loss are predominant after the systole, furthermore, the cross-sectional cut-planes reveal that energy loss, in the wake of systole, prevails toward the vessel wall, whereas, after the diastole, energy loss is focused on the central zone.

3.2 Post-processing Results: Displacement Forces

Displacement Forces acting on the stent-grafts are accused to be one of the principal causes of devices migration, so their failure, because of this it was interesting to analyse them.

Displacement Forces were calculated as the sum of the net pressure, locally normal to the vessel wall, and the wall shear stress both integrated on surface domain. DFs, as previously done for the VDR, were examined for the entire models, but also for bodies and branches, on the entire cardiac cycle, on the systole and on the diastole.

Displacement Forces mediated on all the cardiac cycle were calculated separately for the body and both left and right branch, so their magnitude, direction and verse are plotted as follows.

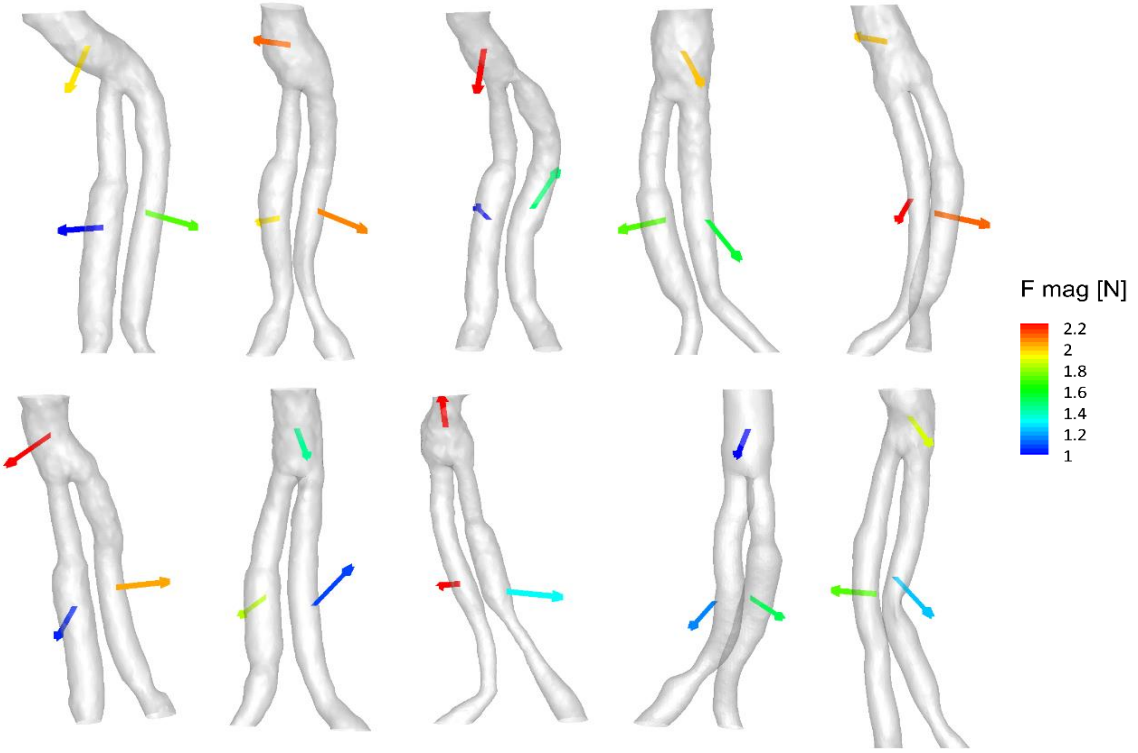

Figure 3.6: vector plots of time-averaged DFs

Taking account on the whole models, DFs, evaluated on all the devices, present a mean value of 1.580±0.647 N on all the cardiac cycle, 1.527±0.622 N on systole and 1.623±0.668 N on diastole. In the same way, mean values of 1.855±0.609 N, 1.784±0.555N and 1.911±0.596 N on body and mean values of 1.61 1±0.320 N,

1.549±0.308 N and 1.661±0.329 N on the branches emerged. Comparable measures on all the examined periods are obtained.

Development of the Displacement Forces over time for a representative case is shown below, it can be noted as this latter properly follows the trend of the pressure over time, it appears, indeed, not affected by the wall shear stress that is two orders of magnitude lower than pressure.

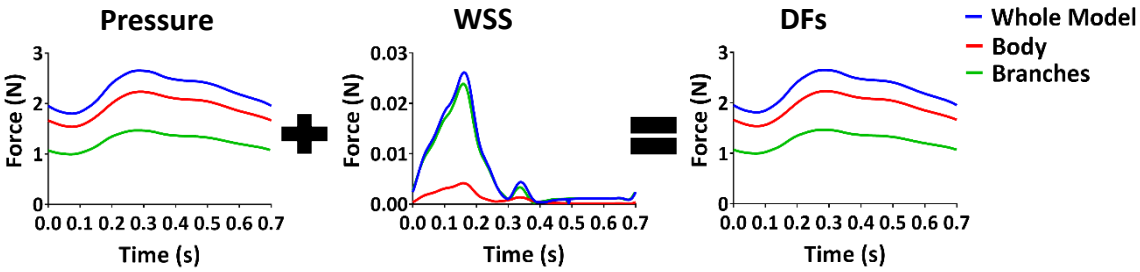

Figure 3.7: Development of Forces over time

Vector plots of the time-averaged Pressures, exercised on the vessel wall of the model, for the first model are reported below:

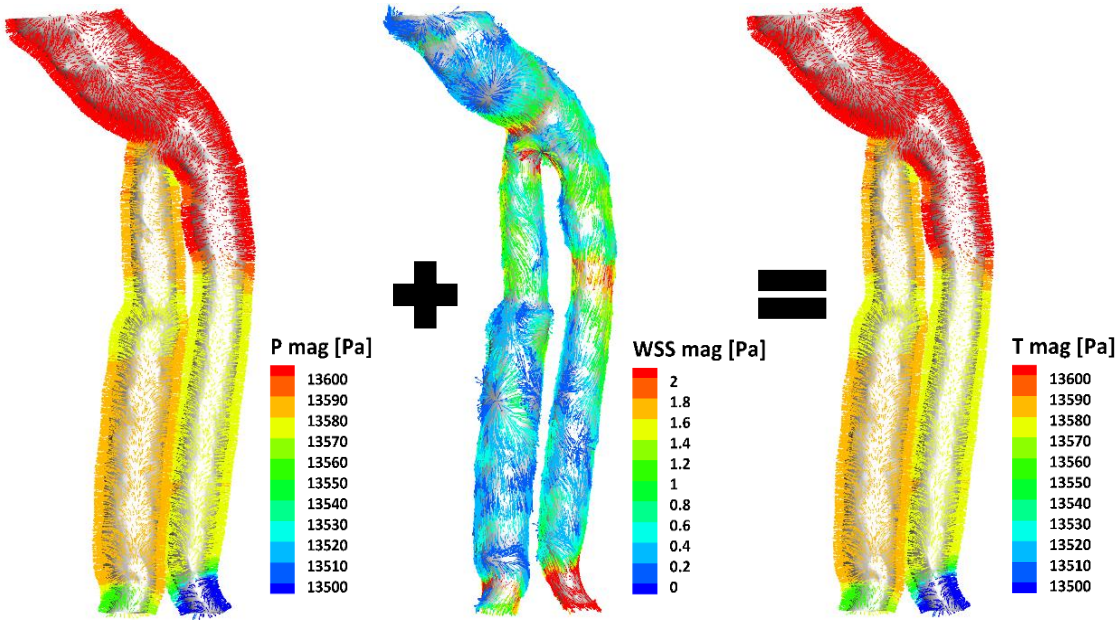

Figure 3.8: time-averaged Forces

As preannounced by literature, it emerges that the main contribution to Displacement Forces originates from the Pressure, these last two have, in fact, same vectors configuration and same order of magnitude.

3.3 Post-processing Results: VDR vs DFs

Displacement Forces have an impact on the stent-grafts stability in EVAR treatment, they can be responsible for device relocation, so failure of this latter; because of it, a possible relation with the Viscous Dissipation Rate was examined. Through statistical analysis, correlation coefficient and P-value were extrapolated and tabulated.

Table 3.1: Correlation between Displacement Forces and Viscous Dissipation Rate in terms of correlation coefficient

	Df_{mean}	**$DF_{systole}$**	**$DF_{diastole}$**	**$DFax_{mean}$**	**$DFax_{systole}$**	**$DFax_{diastole}$**	**DFp_{mean}**	**$DFp_{systole}$**	**$DFp_{diastole}$**
VDR_{tot}	-0,218	-0,222	-0,539	-	-	-	-	-	-
VDR_b	0,527	0,576	**0,648**	0,164	-0,030	0,345	0,164	0,358	0,188
VDR_{bs}	0,331	0,359	-0,008	0,335	0,354	0,113	0,328	0,331	0,030

Note: ρ values with P-value <0.05 were been highlighted

A single statistically significative result was came out, specifically relation between the Viscous Dissipation Rate and the mean Displacement Force in the body was found.

3.4 Post-processing Results: VDR vs GIs

From literature it seems that Geometric Indexes influence the success of the EVAR treatment, for that reason a possible relation with the Viscous Dissipation Rate was studied.

Table 3.2: Correlation between Geometric Indexes and Viscous Dissipation Rate in terms of correlation coefficient

	A_{mean} (cm^2)	**$\lvert R_{mean} \rvert$** (cm)	**C_{mean}** (mm^{-1})	**$\lvert T_{mean} \rvert$** (mm^{-1})	**A_{max}**	**R_{peak}**	**C_{peak}**	**T_{peak}**	**A_{PP}**	**R_{PP}**	**C_{PP}**	**T_{PP}**
VDR_{tot} (J)	-0,299	0,503	0,162	0,281	0,319	0,540	-0,365	-0,418	0,371	**0,723**	-0,368	-0,212
VDR_b	**-0,675**	0,224	0,079	0,382	-0,515	**0,891**	0,527	0,358	0,292	0,442	0,527	0,406
VDR_{bs}	-0,245	-0,099	0,356	0,279	**0,629**	0,207	0,064	0,185	**0,503**	0,433	0,058	0,103

Note: ρ values with P-value <0.05 were been highlighted

For what concerns the entire model, a statistically significative relation between the Viscous Dissipation Rate and the peak-to-peak measure of the variation rate of the area was emerged. Exploring separately body and branches, in the first it turns out that the

mean Area and the peak value of the variation rate of the area are statistically significantly correlated with the Viscous Dissipation Rate, whereas in the seconds, statistically significant correlations were occurred between the maximum Area and the Viscous Dissipation Rate and between the peak-to-peak Area and the Viscous Dissipation Rate. Negative ρ values are an indicator of inverse correlation. It could not say with certainty that correlations are actually meaningful in the body, due to its small size too few points could be to analyse. Where statistically significant correlation was found, scatter plot was used to display values from the two involved variables, then a line of best fit was drawn in order to identify the kind of relation between the variables, consequently linear regression was performed to observe a possible linear relation.

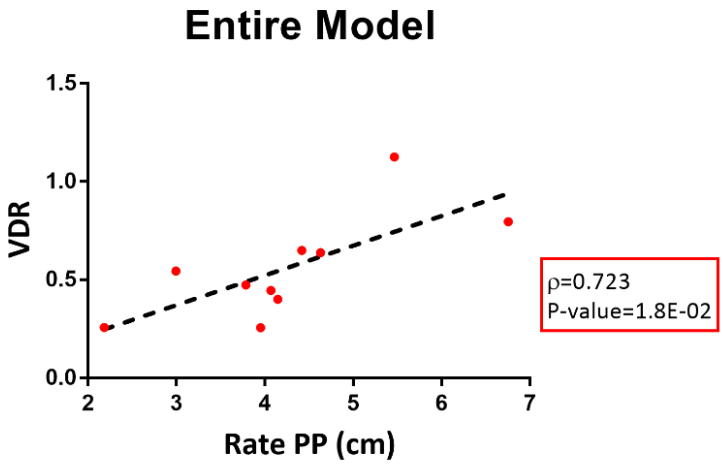

Figure 3.9: scatter plot and best fit line

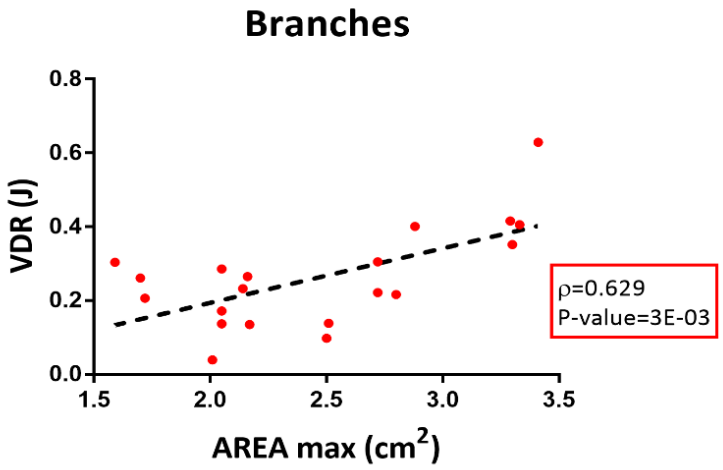

Figure 3.10: scatter plot and best fit line

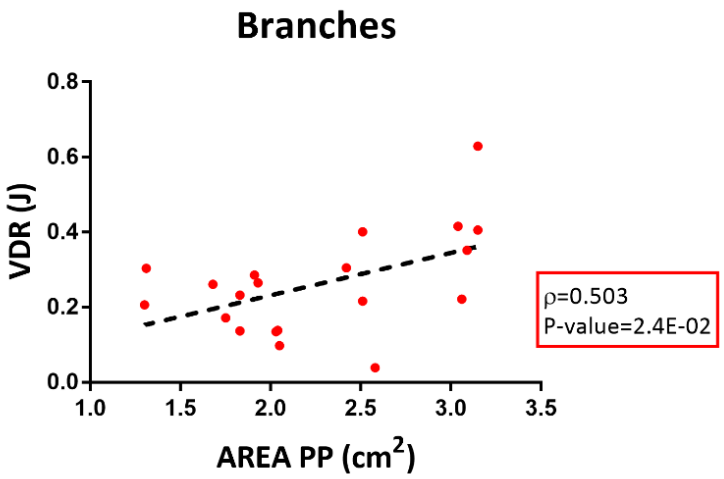

Figure 3.11: scatter plot and best fit line

From graphs it transpires a wide dispersion of the data, they actually much deviate from assuming a linear shape.

3.5 Post-processing results: VDR vs BFIs

It's common knowledge that motion of the fluid dynamics structure is typically spiral-shaped, organized helical motions move and develop through arteries. These emergent behaviours and their topologic aspects are caught from a quantity namely helicity. This latter provides a measure of how a fluid dynamics structure is given from composition of two motion, one along the centreline and the other through plane. It was found that the presence of helicity inside a motion field, particularly in case of turbulent flow, mitigates the energy losses, which is why the bulk flow indexes, descriptors of intravascular structures based on helicity, were analysed and a possible relation between these latter and the Viscous Dissipation Rate was evaluated. Statistical analysis was conducted, and correlation coefficients and P-value were obtained.

Table 3.3: Correlation between intravascular descriptors and Viscous Dissipation Rate on the cycle in terms of correlation coefficient

All Cycle

	h1	h2	h3	h4
VDR_{tot}	-0,055	**0,955**	0,139	0,562
VDR_{b}	0,030	**0,879**	0,042	-0,176
VDR_{bs}	0,294	**0,865**	0,323	0,040

Note: ρ values with P-value <0.05 were been highlighted

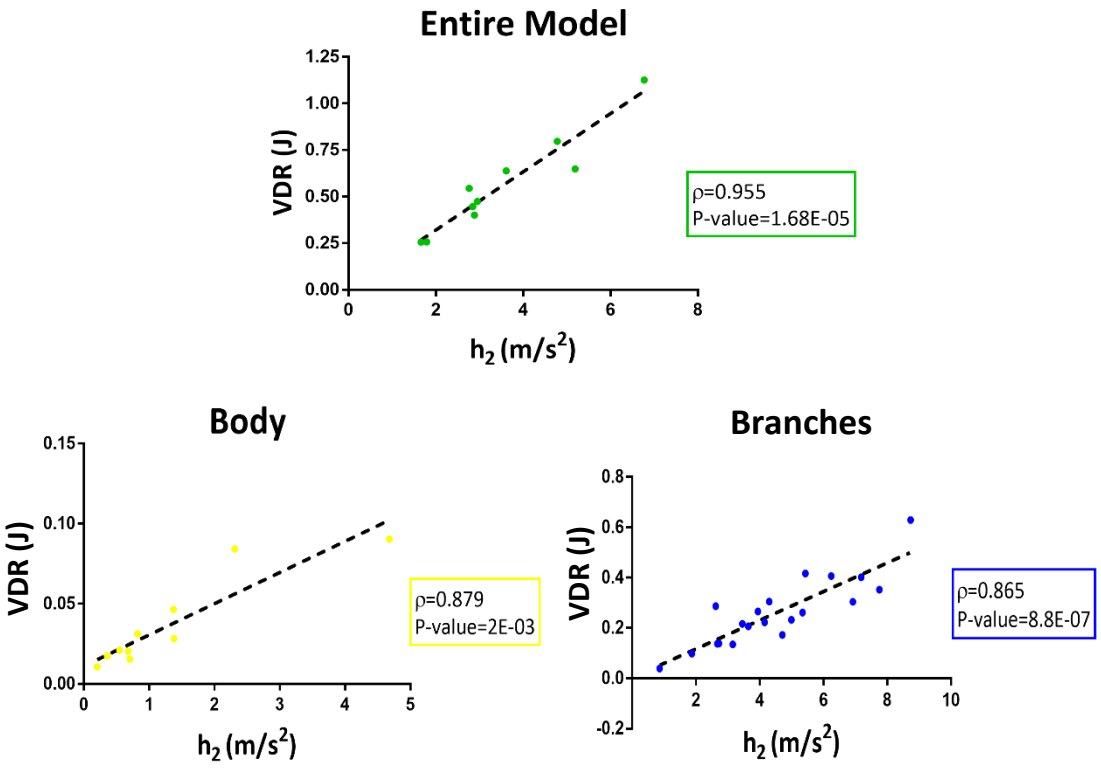

Figure 3.12: scatter plots and best fit lines for the whole cardiac cycle

Table 3.4: Correlation between intravascular descriptors and Viscous Dissipation Rate on systole in terms of correlation coefficient

Systole

	h1	h2	h3	h4
VDR_{tot}	0,450	0,942	0,511	0,237
VDR_b	0,115	0,891	-0,042	-0,273
VDR_{bs}	0,095	0,867	0,526	-0,092

Note: ρ values with P-value <0.05 were been highlighted

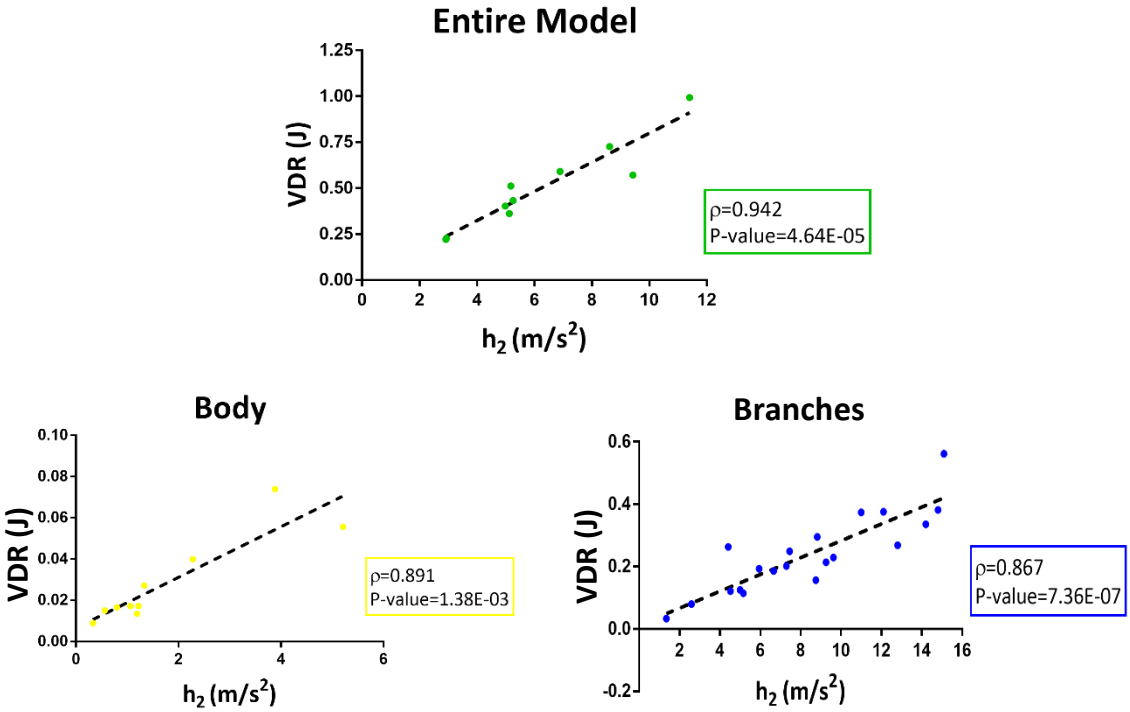

Figure 3.13: scatter plots and best fit lines for the systole

Table 3.5: Correlation between intravascular descriptors and Viscous Dissipation Rate on systole in terms of correlation coefficient

Diastole

	h1	h2	h3	h4
VDR_{tot}	0,224	**0,927**	0,248	0,406
VDR_b	0,248	**0,952**	0,273	0,188
VDR_{bs}	-0,373	**0,487**	-0,376	-0,179

Note: ρ values with P-value <0.05 were been highlighted

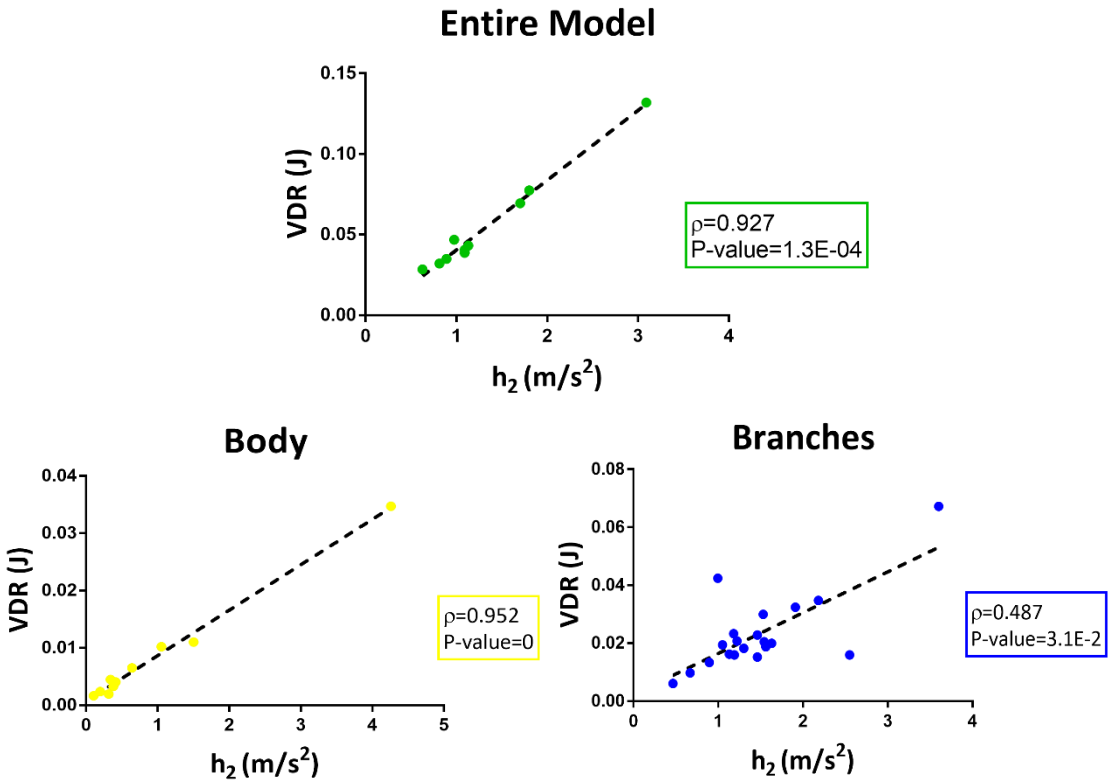

Figure 3.14: scatter plots and best fit lines for the diastole

From tables and graphs, it is distinctly noticeable that in all cases the Viscous Dissipation Rate on the entire model, on body and on branches is hardly positive correlated with the Helicity intensity h_2, in fact, looking at scatter plot, employed to visualise values from involved variables, and the best fit line obtained from the linear regression, strong association was found, data slavishly follow a linear shape, in particular in the entire model and in the body.

3.6 Post-processing results: DFs vs GIs

Displacement Forces result to be associated positively with the mean torsion in absolute terms in the body, whereas in branches correlations of the DFs with Area, Curvature and Torsion are found.

Table 3.6: Correlation between Displacement Forces and Geometric descriptors in terms of correlation coefficient

C_{mean}	$\lvert T_{mean} \rvert$	A_{max}	R_{peak}	C_{peak}	T_{peak}	A_{PP}	R_{PP}	C_{PP}	T_{PP}
-0,122	-0,127	-0,326	-0,411	-0,067	0,394	-0,375	-0,509	-0,054	0,382
-0,261	0,648	-0,018	0,406	0,176	-0,273	0,383	0,115	0,176	-0,139
0,611	0,247	0,593	0,328	0,152	0,365	0,555	0,338	0,150	0,455

Note: ρ values with P-value <0.05 were been highlighted

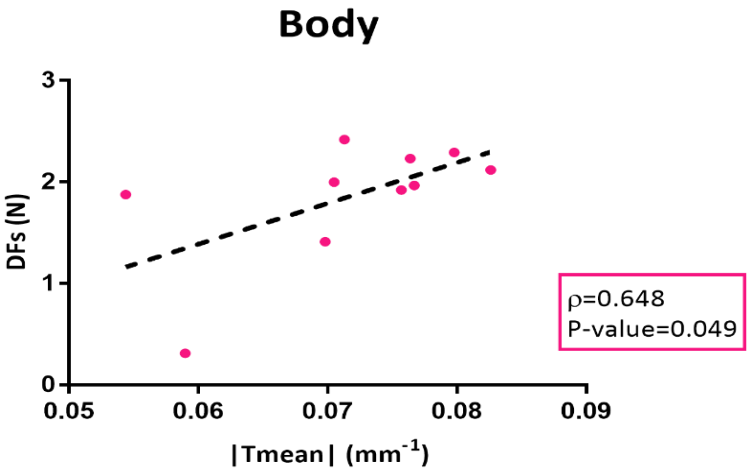

Figure 3.15: scatter plot and best fit line

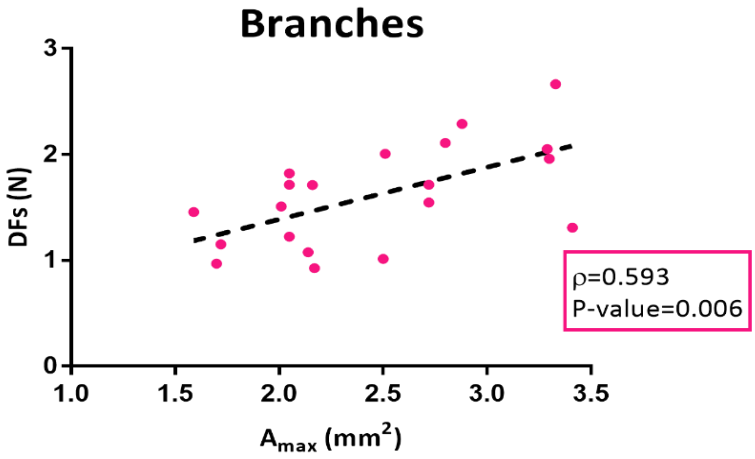

Figure 3.17: scatter plot and best fit line

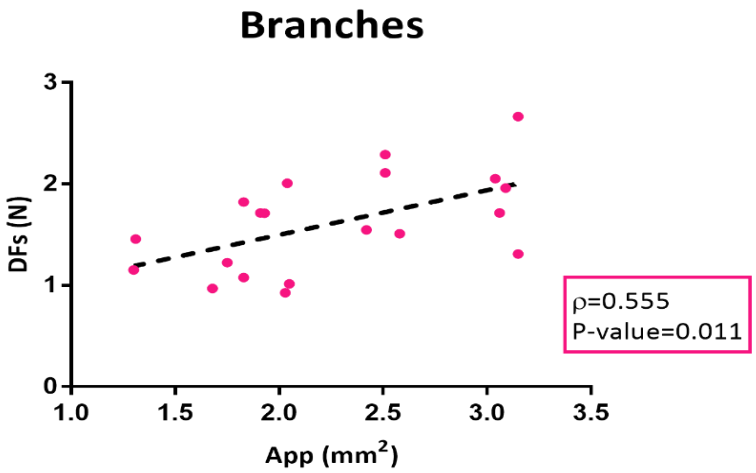

Figure 3.16: scatter plot and best fit line

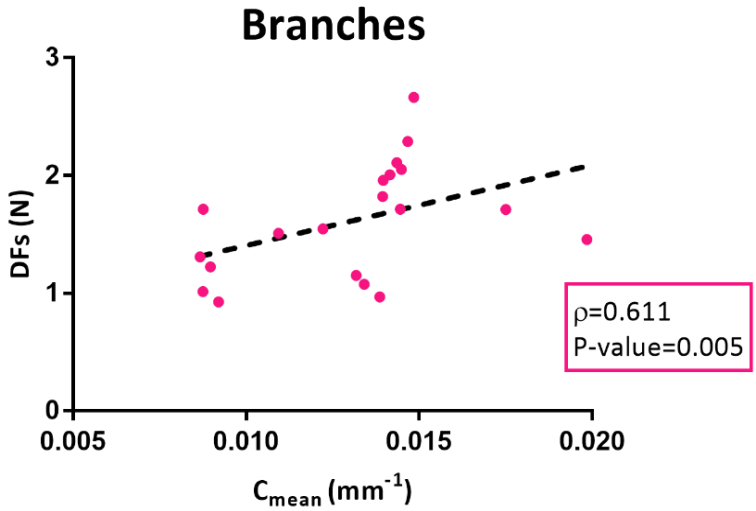

Figure 3.18: scatter plot and best fit line

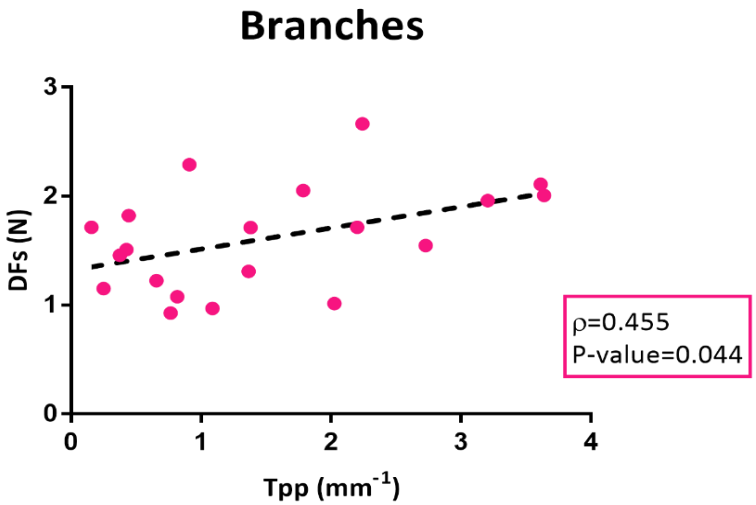

Figure 3.20: scatter plot and best fit line

3.7 Post-processing results: DFs vs BFIs

Possible relation between Displacement Forces and intravascular flow descriptors was inferred, revealing an association, specifically with the ratio between the mean helicity in absolute terms and the helicity intensity, inverse during systole but positive during diastole in branches.

Table 3.7: Correlation between DFs and intravascular descriptors on systole in terms of correlation coefficient

Systole

	h1	h2	h3	h4
DF_{tot}	-0,336	-0,444	-0,518	0,458
DF_b	-0,212	0,442	-0,285	0,212
DF_{bs}	0,050	0,282	0,144	-0,504

Note: ρ values with P-value <0.05 were been highlighted

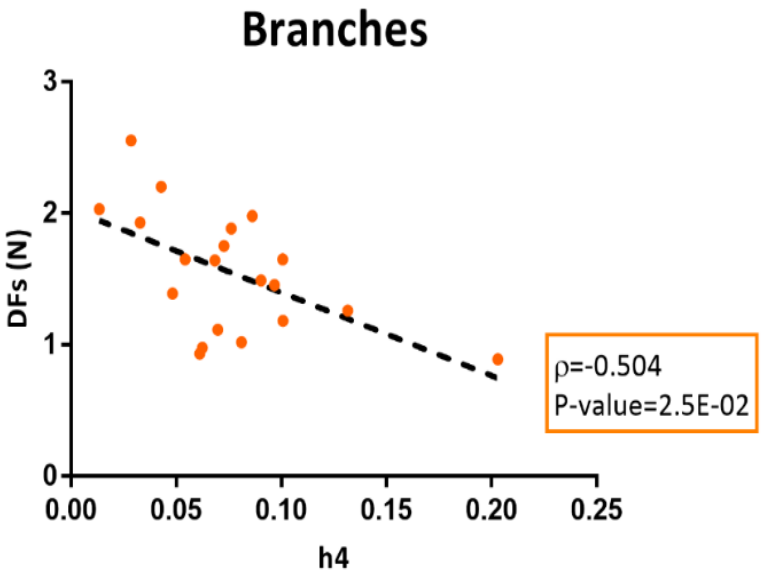

Figure 3.21: scatter plot and best fit line for the systole

Table 3.8: Correlation between DFs and intravascular descriptors on systole in terms of correlation coefficient

Diastole

	h1	h2	h3	h4
DF_{tot}	0,164	-0,467	0,236	-0,437
DF_b	0,321	0,624	0,382	0,248
DF_{bs}	0,196	-0,320	0,075	0,484

Note: ρ values with P-value <0.05 were been highlighted

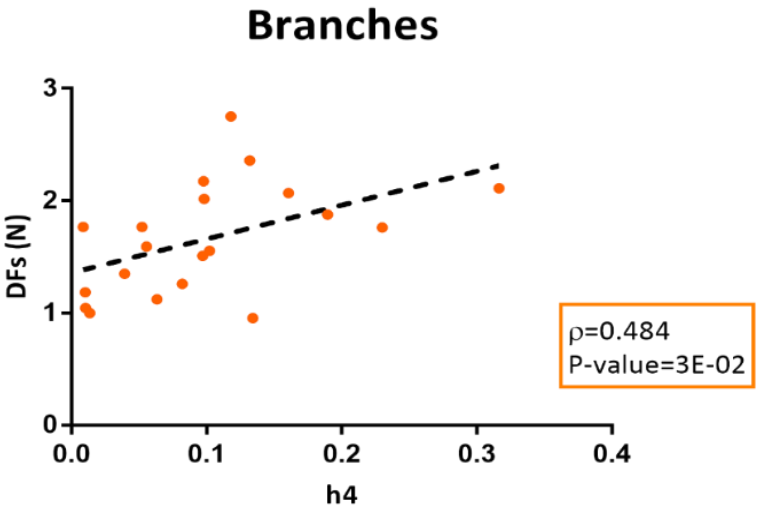

Figure 3.22: scatter plot and best fit line for the diastole

Chapter 4

Conclusions

In this last chapter the main conclusions about this study are identified. Evidences emerging from Viscous Dissipation Rate analysis in different conditions and regions of the models was reported, then results from Displacement Forces analysis was discussed and, in addition, more relevant outcomes generated from statistical analysis were discussed.

Endovascular surgery it is a confirmed clinical practice largely applied thanks to its low invasiveness. Instead of many advantages, EVAR devices presents some complications in short and long-term stability. The implanted device modifies the physiological hemodynamics that could bring to device failure.

The aim of this study was to evaluate the evolution of energy loss by means of the Viscous Dissipation Rate in ten patient-specific endovascular graft models of patients treated Gore Medical Excluder® devices, subsequently it was interesting to analyse the Displacement Forces acting on the stent-grafts accused be one of the principal causes of devices migration, so their failure.

Possible associations of between Viscous Dissipation Rate and Displacement Forces with Geometric and intravascular flow descriptors, that could influence the correct functionality of the device and its stability, were verified.

First of all, it clearly results that power losses, derived from the integration of Viscous Dissipation Rate on volume of interest, are dominant in the systolic phase of the cardiac cycle in the entire device. As consequence, the mean energy dissipation, calculated considering all the whole models, after systole seems to be much more relevant compared to the mean energy dissipation after diastole, in fact mean value is equal to 0.558 ± 0.249 J on all cardiac cycle, 0.504 ± 0.222 J on the systole and 0.054 ± 0.030 J on diastole; same behavior is found analyzing separately its segments.

It is also noticeable that predominant contribution of energy losses always arising from branches, whereas the contribution deriving from the body is almost negligible. An appreciable difference is found in spatial distribution of the maximum values of energy loss after systole and diastole, in the first case the higher values of energy loss are toward the vessel wall, in the second case in the central region.

Furthermore, a detailed study conducted on the DFs demonstrated, as previous works did, that they are mainly due to the pressure rather than the wall shear stress, they indeed can be comparable, in terms of orders of magnitude, with the pressure. DFs, evaluated on all the models, present a mean value of 1.58±0.65 N on all the cardiac cycle, 1.527 ± 0.622 N on the systole and 1.623 ± 0.668 N in the diastole.

Secondly, from statistical analysis it appears that a single statistically significative result was came out comparing the VDR and the DFs, these two are, in fact, correlated in the body after diastole. For what concerns correlation between the VDR and the geometric indexes of the stent-grafts, in the entire model a statistically significative relation between the Viscous Dissipation Rate and the peak-to-peak measure of the variation rate of the area is emerged, then exploring separately body and branches, in the first it turns out that the mean Area and the peak value of the variation rate of the area are statistically significantly correlated with the Viscous Dissipation Rate, whereas in the seconds, statistically significant correlations were occurred between the maximum Area and the Viscous Dissipation Rate and between the peak-to-peak Area and the Viscous Dissipation Rate.

Displacement Forces are associated with geometric descriptors, as torsion in the body and area, curvature and torsion in the branches, and with hemodinamics descriptors in branches on systole and diastole.

The most remarkable outcome occurs when the Viscous Dissipation Rate is associated to the intravascular descriptors, indeed, in all the cases VDR is strongly positively correlated with the Helicity intensity. These findings suggest that dissipation rate is hardly linked to the topology of fluid dynamics structures and to their evolution through the cardiac cycle.

Study results highlight necessity to evaluate, at the design stage, geometry and the hemodynamics of stent-grafts to optimize them and to predict their long-term stability.

allVDR.py

```
import time
from tqdm import tqdm
import numpy as np

mu=3.5e-3 #Pa.s
VDRv=numpy.zeros((200,1))

volume=numpy.loadtxt('volume_EX1.dat')



file=open('dv_noFE201.tec','r')
v=file.readlines()
a = v[1].split(',')
N = int(a[0].split('=')[1])
E = int(a[1].split('=')[1])
con_matr=np.zeros((E,4))
bb=np.zeros((N,15))
coordinates=np.zeros((N,3))
VDRtot=np.zeros((N,200))
VDRtotpoint=np.zeros((N,200))
VDRbb=np.zeros((200,6))

for g in range(E):
   con_matr[g, :]=v[g+2+N].split(' ')

for m in range(N):
   bb[m,:]=v[m+2].split(' ')
coordinates=bb[:,0:3]
```

```
index_body=np.array(np.where(bb[:,5]==0))
volume_body=volume[index_body]

index_branch1=np.array(np.where(bb[:,5]==2))
index_branch2=np.array(np.where(bb[:,5]==3))
index_branches=np.concatenate((index_branch1, index_branch2), axis=1)
volume_branches=volume[index_branches]



for n in range(201,401):
    num=str(n)
    file_open=open('dv_noFE'+num+'.tec','r')
    velocity=file_open.readlines()

    a = velocity[1].split(',')
    N = int(a[0].split('=')[1])
    E = int(a[1].split('=')[1])
    b = np.zeros((N, 15))
    for i in range(N):
        b[i, :]=velocity[i+2].split(' ')
    c=np.zeros((N, 9))
    c=b[:,6:16]
    VDRpoint=np.zeros((N,1))
    VDR=np.zeros((N,1))



    for z in range(N):
        VDRpoint[z]=mu*(2*(c[z,8]**2+c[z,4]**2+c[z,0]**2)+
        +(c[z,7]+c[z,5])**2+(c[z,6]+c[z,2])**2+(c[z,1]+c[z,3])**2)
```

```
    VDR[z]=VDRpoint[z]*volume[z]
  VDR=np.reshape(VDR,(N,))
  VDRpoint=np.reshape(VDRpoint,(N,))
VDRtot[:,n-201]=VDR
VDRtotpoint[:,n-201]=VDRpoint


VDR_body=np.zeros((len(index_body),1))
VDR_body=mu*(2*(c[index_body,8]**2+c[index_body,4]**2+c[index_body,0]**2)+
+(c[index_body,7]+c[index_body,5])**2+(c[index_body,6]+c[index_body,2])**2+
+(c[index_body,1]+c[index_body,3])**2)
VDR_body=VDR_body*volume_body

VDRbb[n-201,0]=np.sum(VDR_body)
VDRbb[n-201,1]=np.sum(VDR_body)/np.sum(volume_body)


VDR_branches=np.zeros((len(index_branches),1))
VDR_branches=mu*(2*(c[index_branches,8]**2+c[index_branches,4]**2+
+c[index_branches,0]**2)+(c[index_branches,7]+c[index_branches,5])**2+
+(c[index_branches,6]+c[index_branches,2])**2+(c[index_branches,1]+
+c[index_branches,3])**2)
VDR_branches=VDR_branches*volume_branches

VDRbb[n-201,2]=np.sum(VDR_branches)
VDRbb[n-201,3]=np.sum(VDR_branches)/np.sum(volume_branches)

VDRbb[n-201,4]=np.sum(VDR_branches)+np.sum(VDR_body)
VDRbb[n-201,5]=(np.sum(VDR_branches)+np.sum(VDR_body))/
/(np.sum(volume_branches)+np.sum((volume_body)))
```

```
#il VDR rappresenta la quantità dissipata
#VDRtot matrice (N,num_timestep), la somma delle righe da il VDR del
#volume totale per ogni time step, diventa un vettore(1,200), la somma
#delle colonne da un vettore(N,1) che sarebbe il VDR sull'intero ciclo
#cardiaco per ogni nodo

ts=200
VDR_ontime=np.zeros((N,1))
VDR_ontime=np.sum(VDRtot, axis=1)
VDR_ontime=np.reshape(VDR_ontime, (N,1))

txt_VDRonvolume='VARIABLE=VDRbody, VDRbody_norm, VDRbranches,
VDRbranches_norm, VDRtot, VDRtot_norm \n'
for l in range(ts):
   for w in range(6):
      txt_VDRonvolume=txt_VDRonvolume + '%e ' %(VDRbb[l][w])
   txt_VDRonvolume=txt_VDRonvolume+ '\n'

k=open('VDR_onvolume.dat','w')
k.write(txt_VDRonvolume)
k.close()

txt_VDRtot=''
for h in range(N):
   for z in range(ts):
      txt_VDRtot=txt_VDRtot+'%e ' %(VDRtot[h,z])
   txt_VDRtot=txt_VDRtot+'\n'

q=open('VDRvolume_time.dat','w')
q.write(txt_VDRtot)
```

```
q.close()


line1='VARIABLES= X, Y, Z, VDR_ONTIME, ID \n'

line2='ZONE N=' +str(N)+', E=' +str(E)+ ', F=FEPOINT,ET=TETRAHEDRON \n'


txt_VDRplot=line1+line2

for l in tqdm(range(N)):

   txt_VDRplot=txt_VDRplot+ '%e %e %e %e %f \n' %(coordinates[l,0], coordinates[l,1], coordinates[l,2], VDR_ontime[l,0], b[l,5])


for l in tqdm(range(E)):

   txt_VDRplot=txt_VDRplot+ '%i %i %i %i \n' %(con_matr[l,0], con_matr[l,1], con_matr[l,2], con_matr[l,3])


p=open('VDR_plot.tec','w')

p.write(txt_VDRplot)

p.close()
```

VDR_sys_dia.py

```
import time

from tqdm import tqdm

import numpy as np


allVDR=np.loadtxt('VDRvolume_time.dat')

file=open('VDR_plot.tec','r')

v=file.readlines()

a = v[1].split(',')

N = int(a[0].split('=')[1])
```

```
E = int(a[1].split('=')[1])
con_matr=np.zeros((E,4))
coordinates=np.zeros((N,3))
VDR_sys=np.zeros((N,89))
VDR_dia=np.zeros((N, 111))
ID=np.zeros((N,1))

for m in range(N):
    t=v[m+2].split(' ')
    coordinates[m,:]=t[0:3]
    ID[m,:]=t[4]

for g in range(E):
    p=v[g+2+N].split(' ')
    con_matr[g, :]=p[0:4]

VDR_sys=allVDR[:,0:89]
VDR_dia=allVDR[:, 89:201]

VDR_sys_time=np.sum(VDR_sys, axis=1)
VDR_sys_time=np.reshape(VDR_sys_time, (N,1))

VDR_dia_time=np.sum(VDR_dia, axis=1)
VDR_dia_time=np.reshape(VDR_dia_time, (N,1))

line1='VARIABLES= X, Y, Z, VDR_ONTIME, ID \n'
line2='ZONE N=' +str(N)+', E=' +str(E)+ ', F=FEPOINT,ET=TETRAHEDRON \n'

txt_VDR_sys_plot=line1+line2
for l in tqdm(range(N)):
```

```
    txt_VDR_sys_plot=txt_VDR_sys_plot+ '%e %e %e %e %f \n' %(coordinates[l,0],
coordinates[l,1], coordinates[l,2], VDR_sys_time[l,0], ID[l,0])

for l in tqdm(range(E)):

    txt_VDR_sys_plot=txt_VDR_sys_plot+ '%i %i %i %i \n' %(con_matr[l,0], con_matr[l,1],

    con_matr[l,2], con_matr[l,3])


q=open('VDR_sys_plot.tec','w')

q.write(txt_VDR_sys_plot)

q.close()


txt_VDR_dia_plot=line1+line2

for l in tqdm(range(N)):

    txt_VDR_dia_plot=txt_VDR_dia_plot+ '%e %e %e %e %f \n' %(coordinates[l,0],
coordinates[l,1], coordinates[l,2], VDR_dia_time[l,0], ID[l,0])


for l in tqdm(range(E)):

    txt_VDR_dia_plot=txt_VDR_dia_plot+ '%i %i %i %i \n' %(con_matr[l,0], con_matr[l,1],
con_matr[l,2], con_matr[l,3])


z=open('VDR_dia_plot.tec','w')

z.write(txt_VDR_dia_plot)

z.close()
```

Bibliography

[1] **http://www.innerbody.com/image/card01.html**

[2] **https://opentextbc.ca/anatomyandphysiology/chapter/20-1-structure-and-function-of-blood-vessels/**

[3] **BSCV 2017/2018**

[4] Ouriel K, Green RM, Donayre C, et al**. An evaluation of new methods of expressing aortic aneurysm size: relationship to rupture**. J Vasc Surg 1992; 15: 12–20.

[5] BRIAN KEISLER, MD, and CHUCK CARTER, MD, **Abdominal Aortic Aneurysm**, University of South Carolina School of Medicine, Columbia, South Carolina.

[6] Chang M. He, MSc, and Margot R. Roach, MD, Phi), **The composition and mechanical properties of abdominal aortic aneurysms**, London, Ontario, Canada.

[7] N Sakalihasan, R Limet, O D Defawe, **Abdominal aortic aneurysm**.

[8] F.L. Moll, J.T. Powell, G. Fraedrich, F. Verzini, S. Haulon, M. Waltham, J.A. van Herwaarden, P.J.E. Holt, J.W. van Keulen, B. Rantner, F.J.V. Schlo¨sser, F. Setacci, J.-B. Ricco, **Management of Abdominal Aortic Aneurysms Clinical Practice Guidelines of the European Society for Vascular Surgery**.

[9] Nikolaos Kontopodis, Eleni Metaxa, Yannis Papaharilaou, Emmanouil Tavlas, Dimitrios Tsetis and Christos Ioannou, **Advancements in identifying biomechanical determinants for abdominal aortic aneurysm rupture**.

[10] A. K. Venkatasubramaniam, M. J. Fagan, T. Mehta, K. J. Mylankal, B. Ray, G. Kuhan, I. C. Chetter and P. T. McCollum, **A Comparative Study of Aortic Wall Stress Using Finite Element Analysis for Ruptured and Non-ruptured Abdominal Aortic Aneurysms**; *Academic Vascular Unit, Vascular Laboratory, Alderson house, Hull Royal Infirmary, Hull, East Yorkshire HU3 2JZ, UK.*

[11] Michael S. Heng, MRCS, Michael J. Fagan, PhD, Jason W. Collier, PhD, Grishma Desai, PhD, Peter T. McCollum, MCh, and Ian C. Chetter, MD, **Peak wall stress measurement in elective and acute abdominal aortic aneurysms**, *Hull, United Kingdom.*

[12] C. Alberto Figueroa and Christopher K. Zarins **Computational Analysis of Displacement Forces Acting on Endografts Used to Treat Aortic Aneurysms**.

[13] Bao-Ngoc Nguyen, MD, Richard F. Neville, MD, Rodeen Rahbar, MD, Richard Amdur, PhD, and Anton N. Sidawy, MD, MPH, **Comparison of Outcomes for Open Abdominal Aortic Aneurysm Repair and Endovascular Repair in Patients With Chronic Renal Insufficiency**.

[14] **Endovascular aneurysm repair versus open repair in patients with abdominal aortic aneurysm (EVAR trial 1): randomised controlled trial**

[15] Dustin Thomas, David Anderson1, Edward Hulten, Fiora McRae, Shane Ellis, Jamil A Malik, Todd C Villines and Ahmad M Slim, **Open versus endovascular repair of abdominal aortic aneurysm: Incidence of cardiovascular events in 632 patients in a department of defense cohort over 6-year follow-up**.

[16] C. Alberto Figueroa and Christopher K. Zarins, **Computational Analysis of Displacement Forces Acting on Endografts Used to Treat Aortic Aneurysms**.

[17] Irwin V. Mohan, FRCS; Peter L. Harris, FRCS; Corine J. van Marrewijk, PhD; Robert J. Laheij, PhD; and Thien V. How, **Factors and Forces Influencing Stent-Graft Migration After Endovascular Aortic Aneurysm Repair**, MD, *Royal Liverpool University Hospital and Department of Clinical Engineering, University of Liverpool, England, UK; EUROSTAR Data Registry Centre, Eindhoven, The Netherlands.*

[18] Kandail, H., et al., **Patient-specific analysis of displacement forces acting on fenestrated stent grafts for endovascular aneurysm repair. Journal of Biomechanics (2014)**, http://dx.doi.org/10.1016/j.jbiomech.2014.08.011

[19] C. Alberto Figueroa, PhD; Charles A. Taylor, PhD; Victoria Yeh; Allen J. Chiou; and Christopher K. Zarins, MD, **Effect of Curvature on Displacement Forces Acting on Aortic Endografts: A 3-Dimensional Computational Analysis**, *Departments of Bioengineering and Surgery, Stanford University, Stanford, California, USA.*

[20] Zhenglun Alan Wei, Michael Tree, Phillip M. Trusty, Wenjun Wu, Shelly Singh-Gryzbon, and Ajit Yoganathan, *Wallace H.,* **The Advantages of Viscous Dissipation Rate over Simplified Power Loss as a Fontan Hemodynamic Metric**, *Coulter School of Biomedical Engineering, Georgia Institute of Technology, Atlanta, GA 30332, USA; George W. Woodruff School of Mechanical Engineering, Georgia Institute of Technology, Atlanta, GA, USA; and Institute of Computational Science and Cardiovascular Disease, Nanjing Medical University, Nanjing, China, 2017*

[21] Paola Tasso, Anastasios Raptis, Mitiadis Matsagkas, Maurizio Lodi Rizzini, Diego Gallo, Michalis Xenos, Umberto Morbiducci, 2018, **Abdominal Aortic Aneurysm Endovascular Repair: Profiling Postimplantation Morphometry and Hemodynamics With Image-Based Computational Fluid Dynamics,** Journal of Biomechanical Engineering

[22] Olufsen, M. S., Peskin, C. S., Kim, W. Y., Pedersen, E. M., Nadim, A., and Larsen, J., 2000, **Numerical Simulation and Experimental Validation of Blood Flow in Arteries With Structured-Tree Outflow Conditions**, Ann. Biomed. Eng., 28(11), pp. 1281–1299.

[23] Gallo, D., Lefieux, A., Morganti, S., Veneziani, A., Reali, A., Auricchio, F., Conti, M., and Morbiducci, U., 2016, "**A Patient-Specific Follow Up Study of the Impact of Thoracic Endovascular Repair (Tevar) on Aortic Anatomy and on Post-Operative Hemodynamics**," Comput. Fluids, 141, pp. 54–61.

[24] Gallo, D., Vardoulis, O., Monney, P., Piccini, D., Antiochos, P., Schwitter, J., Stergiopulos, N., and Morbiducci, U., 2017, "**Cardiovascular Morphometry With High-Resolution 3d Magnetic Resonance: First Application to Left Ventricle Diastolic Dysfunction**," Med. Eng. Phys., 47, pp. 64–71.

[25] Shapiro, S. S., and Wilk, M. B., 1965, "**An Analysis of Variance Test for Normality (Complete Samples)**," Biometrica Trust, 52, pp. 591–611.

[26] H. B. Mann and D.R. Whitney, 1947, "**On a test of whether one of two random variables is stochastically larger than the other**", Ohio State University.